Comparing approaches for numerical modelling of tsunami generation by deformable submarine slides

Rebecca C. Smith[a], Jon Hill[a,b], Gareth S. Collins[a], Matthew D. Piggott[a,c], Stephan C. Kramer[a], Samuel D. Parkinson[a], Cian Wilson[d]

[a] *Applied Modelling and Computation Group, Department of Earth Science and Engineering, Imperial College London, SW7 2AZ, UK.*
[b] *Environment Department, University of York, Heslington, York, YO10 5DD, UK*
[c] *Grantham Institute for Climate Change, Imperial College London, SW7 2AZ, UK*
[d] *Lamont-Doherty Earth Observatory, Columbia University, Palisades, NY 10964, USA*

Email address: `rebecca.smith08@imperial.ac.uk` (Rebecca C. Smith)

Abstract

Tsunami generated by submarine slides are arguably an under-considered risk in comparison to earthquake-generated tsunami. Numerical simulations of submarine slide-generated waves can be used to identify the important factors in determining wave characteristics. Here we use Fluidity, an open source finite element code, to simulate waves generated by deformable submarine slides. Fluidity uses flexible unstructured meshes combined with adaptivity which alters the mesh topology and resolution based on the simulation state, focussing or reducing resolution, when and where it is required. Fluidity also allows a number of different numerical approaches to be taken to simulate submarine slide deformation, free-surface representation, and wave generation within the same numerical framework. In this work we use a multi-material approach, considering either two materials (slide and water with a free surface) or three materials (slide, water and air), as well as a sediment model (sediment, water and free surface) approach. In all cases the slide is treated as a viscous fluid. Our results are shown to be consistent with laboratory experiments using a deformable submarine slide, and demonstrate good agreement when compared with other numerical models. The three different approaches for simulating submarine slide dynamics and tsunami wave generation produce similar waveforms and slide deformation geometries. However, each has its own merits depending on the application. Mesh adaptivity is shown to be able to reduce the computational cost without compromising the accuracy of results.
Keywords:

Submarine Slide, Tsunami, Numerical Modelling, Validation, Adaptive Mesh

1. Introduction

Recent large seismically generated tsunami events, for example the 2004 Indian Ocean, and the 2011 Tohoku events, have highlighted the devastating social and economic effects that tsunami can have. Although these tsunami were seismogenic in origin, submarine mass movements can also generate highly destructive waves (Assier-Rzadkiewicz et al., 2000; Fine et al., 2005; Masson et al., 2006; Dan et al., 2007; Tappin et al., 2008; Tappin, 2010; Bondevik et al., 2005a). Submarine mass movements are more frequently termed submarine slides, even when the mode of deformation is unknown. Here we use submarine slide as a generic term, without reference to the mechanism of movement. When referring to the submarine slide in the models and experiments described here (sections 2–5), we drop the word submarine for brevity, and use 'slide'.

In 1998, the Papua New Guinea submarine slide resulted in a tsunami that devastated coastal villages and killed over 2,100 people (Kawata et al., 1999; Synolakis et al., 2002). A large submarine slide, the Storegga Slide, occurred offshore Norway approximately 8.2 ka (Bugge et al., 1988; Dawson et al., 1988; Smith et al., 2004; Bondevik et al., 2005a; Wagner et al., 2007). The submarine slide volume is estimated at 2400–3200 km^3 and its deposit extended 800 km down slope (Bugge et al., 1988; Gauer et al., 2005; Haflidason et al., 2004, 2005). Deposits from the resulting tsunami indicate vertical run ups (maximum inundation above sea level of a wave incident to a beach) of approximately 3–4 m at the Scottish mainland coast, and over 20 m at the Shetlands Islands and Norwegian coast (Bondevik et al., 2005a,b; Dawson et al., 1988; Smith et al., 2004; Wagner et al., 2007).

Submarine slide events are difficult to predict, monitor or directly observe (Harbitz et al., 2014), therefore research has focused on experimental studies and numerical models. These aim to gain a better understanding of the processes involved and the factors that are important for wave generation. Numerical models in principle allow for the replication of events at realistic scale, but should be validated against field observations where possible, and at the laboratory scale against experimental data. Experiments, in both pseudo-two and three dimensions, have used a number of methods to simulate the submarine slide such as rigid blocks (Heinrich, 1992; Watts, 1998, 2000; Watts et al., 2000; Enet et al., 2003; Grilli and Watts, 2005; Enet and Grilli, 2005; Liu et al., 2005; Sue et al., 2006; Enet and Grilli, 2007; Sue et al., 2011; Whittaker et al., 2012) made of different materials (to alter slide density) and with different slide shapes (e.g. triangular/wedge, elliptical, Gaussian); granular materials (Assier-Rzadkiewicz et al., 1997; Watts and Grilli, 2003; Ataie-Ashtiani and Najafi-Jilani, 2008); and confined granular materials (Ataie-Ashtiani and Najafi-Jilani, 2008). These experiments investigated the effects of various slide parameters (block shape, density, grain size, confinement, submergence, slope angle) on the resulting wave characteristics (amplitude, run up, wave form, dispersion, wave period, wave energy conversion). Some studies using deformable slides have investigated the effect of different grain sizes (e.g. 50 μm – 9 mm by Watts and Grilli (2003); Assier-Rzadkiewicz et al. (1997); Ataie-Ashtiani and Najafi-Jilani (2008)). There have been few studies that have directly investigated the effect of deformable slide rheology on wave generation, although Watts and Grilli (2003); Elverhøi et al. (2005, 2010) and Breien et al. (2010) considered the effect of rheology on slide deformation and dynamics.

The modelling of submarine slide-tsunami from the initiation of submarine slide motion and wave generation, through to wave propagation and inundation in three dimensions is computationally challenging. Moreover, numerical simulations of each stage have tended to rely on simplifications to make the problem more tractable.

One such simplification is to model the slide as a rigid block that cannot deform. However, in reality submarine slides deform (Grilli and Watts, 2005), with complex rheology and flow (Løvholt et al., 2015). Deformation may both increase initial acceleration and decrease submarine slide thickness, which have competing effects on wave generation (Watts, 1997; Watts and Grilli, 2003; Ataie-Ashtiani and Najafi-Jilani, 2008). Løvholt et al. (2015) found that deformation was often too slow to influence wave generation, as most of the generation occurs during the initial acceleration phase, before the slide has time to deform. However, they suggested it may prove important for tsunami wave heights in scenarios that were not considered, and recommended further research.

Another common simplification is to prescribe the motion of the submarine slide, yet several studies have concluded that submarine slide acceleration and velocity are key parameters in determining wave characteristics (Harbitz, 1992; Harbitz et al., 2014; Løvholt et al., 2015). Simulating the slide dynamically, including its interaction with the water, internal deformation and drag, ensures a more accurate description of slide acceleration and velocity, but adds substantial computational expense.

Many studies have solved approximations to the full Navier-Stokes equations (such as the shallow-water equations). While such simplifications are often valid, use of non-depth-averaged and non-hydrostatic models allows vertical acceleration to be considered, which can be important for submarine slide tsunami generation in some scenarios.

Accounting more fully for slide deformation and dynamics, and solving the full Navier-Stokes equations, increases the computational cost of numerical simulations of waves generated by submarine slides. A way to minimise this additional expense is to make optimum use of computational resources, for example by exploiting adaptive meshing technology. We describe here the use of Fluidity, an open source, general purpose, computational fluid dynamics, finite element code (Piggott et al., 2008; AMCG, 2015) to recreate two hypothetical two-dimensional submarine slide tsunami scenarios, one at the laboratory scale (after Assier-Rzadkiewicz et al. (1997); Ma et al. (2013)), and one at full scale, situated in the Gulf of Mexico (after Horrillo et al. (2013)).

We show that Fluidity offers several important benefits for submarine slide tsunami modelling. Fluidity can employ a number of different numerical approaches to simulate the submarine slide dynamics and wave generation, within one numerical framework. Fluidity has already successfully modelled wave generation and large-scale propagation from a prescribed rigid block slide (Hill et al., 2014). Here we extend this by modelling wave generation from a deformable submarine slide that moves dynamically as a Newtonian viscous fluid using three different approaches for modelling slide motion and wave generation. The approaches compared are: a sediment model with a free surface (SEDFS); a two-material model: viscous slide and water, with a free surface (MM2FS); and a three-material model: viscous slide, water and air (MM3). In MM3 the response of the ocean surface to the submarine slide movement is represented by the interface between the water and air, whereas MM2FS and SEDFS use a free surface (FS) boundary condition method. SEDFS is described further in Section 3.1.1 and MM2FS and MM3 in 3.1.2. In all approaches the submarine slide movement is driven by the density difference between the submarine slide and water. We show that the three different approaches produce very similar wave amplitudes and waveforms that are consistent with experimental data (at the laboratory scale) and inform comparisons with other numerical models (at laboratory and full scale) that employ different numerical approaches (e.g., Assier-Rzadkiewicz et al., 1997; Ma et al., 2013). We also discuss the merits of each approach for different applications as well as their relative computational expense.

Fluidity also has the benefit that it solves the Navier-Stokes equations on unstructured meshes, which can be fixed (but still multi-scale: Hill et al. (2014)) or fully dynamically adaptive. Adaptive meshes can help to reduce computational cost without losing accuracy (LeVeque and George, 2008; Hill et al., 2012; Hiester et al., 2014; Parkinson et al., 2014; Behrens, 2014). Adaptive meshes change their topology and resolution based on the current simulation state and as such can focus or reduce resolution when and where it is required. By demonstrating that mesh adaptivity provides substantial computational efficiency in the two-dimensional submarine slide simulations presented here, we propose that future application of mesh adaptivity in three dimensions should allow for the simulation of 'Storegga-sized' slides, and generated waves, in three dimensions, as has not previously been possible.

2. Motivation

A number of different numerical approaches have been used to simulate the generation and propagation of submarine slide generated waves. These have guided and motivated the approaches taken here to simulate slide dynamics and wave generation. Several early numerical studies relied on the shallow water (long-wave) approximation which assumes the horizontal scale of the wave motion is considerably larger than the local water depth or vertical scale (Harbitz, 1992; Jiang and LeBlond, 1992, 1993, 1994; Thomson et al., 2001; Fine et al., 1998, 2005; Assier-Rzadkiewicz et al., 2000). Whilst this approximation is generally appropriate for seismogenic tsunami, it may not be appropriate for submarine slide generated waves, which often have shorter wavelengths (Glimsdal et al., 2013; Løvholt et al., 2015). The approximation also neglects frequency dispersion and vertical velocity/acceleration. Studies by Lynett et al. (2003); Grilli and Watts (2005); Løvholt et al. (2008) and Glimsdal et al. (2013) for simulating tsunami propagation, indicate that waves generated by submarine slides can be strongly affected by dispersive effects, particularly for relatively small slides. Boussinesq forms of the depth-averaged equations are also a popular choice that account for wave dispersion. For a review of their use in the context of submarine slide tsunami see Løvholt et al. (2015) and the references therein. Waves generated by extremely large slides are likely to be less dispersive. In order to investigate fully the effects and importance of slide dynamics and deformability on wave generation, the use of full Navier-Stokes models provides a more complete representation than shallow water models, particularly for relatively small slides (Watts and Grilli, 2003; Abadie et al., 2012; Glimsdal et al., 2013; Horrillo et al., 2013). However, such models also introduce additional complexity, such as accurate treatment of the free surface, and computational expense.

Many previous numerical models of submarine slides approximated the slides as rigid-blocks, that moved according to prescribed motion (e.g. Heinrich (1992); Harbitz (1992); Fuhrman and Madsen (2009); Bondevik et al. (2005b); Berndt et al. (2009); Yuk et al. (2006) and Liu et al. (2005)). For example, Harbitz (1992) and Bondevik et al. (2005a) used analytical expressions to define slide position, velocity and acceleration as a function of time. Harbitz (1992) considered a range of slide velocity profiles to account for uncertainties in slide density, rheology and drag. He found that the wave heights in his simulations were strongly dependent on the acceleration of the slide and the maximum slide velocity.

Modelling the slide dynamics removes the need to prescribe motion, but is computationally more expensive. Prescribing the slide motion results in one-way coupling between the slide and water; i.e., the slide movement influences the water, but the water does not affect the slide motion. Two-way coupling is considered in the work Jiang and LeBlond (1992); Fine et al. (1998); Suleimani et al. (2009); Nicolsky et al. (2010), however these all used shallow water models. Jiang and LeBlond (1992) found that effects of two-way coupling are most significant when the slide density is only slightly greater than the density of the water; and when the slide is located at shallow water depths (i.e. slide density is 1.2 times the water density, slide thickness is 0.4 times water depth). These conditions are not normally fulfilled for submarine slides Harbitz et al. (2006). Although section 4.2 considers a submarine slide located in shallow water where two-way coupling is expected to be important.

Some numerical studies have modelled deformable submarine slides. A number of approaches have been taken, such as modelling the slide as a Newtonian, viscous fluid (Jiang and LeBlond, 1992; Fine et al., 2005; Assier-Rzadkiewicz et al., 1997, 2000; Abadie et al., 2010; Horrillo et al., 2013), as a non-Newtonian fluid (e.g. using a Bingham rheology) (Jiang and LeBlond, 1993; Gauer et al., 2006; Assier-Rzadkiewicz et al., 1997), and as a water-sediment mixture (Ma et al., 2013). Some studies show that slide deformation reduces wave amplitudes. These include laboratory experiments by Watts (1997) that indicated wave amplitudes were 50–90% reduced for deformable slides, compared to rigid slides. Ataie-Ashtiani and Najafi-Jilani (2008) found that using a deformable submarine slide reduced wave amplitude by up to 15%, and increased wave period by up to 10%. However, Grilli and Watts (2005) prescribed time-dependant slide deformation and found the inclusion of deformation produced higher wave amplitudes and affected the wavelength of the generated wave. The simulations by Abadie et al. (2010) also indicated that deformable slides produce higher wave amplitudes than rigid blocks slides. For subaerial slides, Morichon and Abadie (2010) report that slide deformability seems to be a "critical parameter" for the generated waves and run-up. In a recent review, Løvholt et al. (2015) assessed the characteristics of submarine slide tsunami and concluded that the initial acceleration of submarine slides is the most important kinematic slide parameter in determining the initial sea surface elevation for slides with a long run-out distance. When slide run-out distance is relatively short compared to the slide length, the velocity of the slide becomes more important. They further concluded that rapid deformation during the initial acceleration phase would be needed to influence the wave produced and recommend further research into slide scenarios with strong deformation. Since slides are always deformable in real cases, Grilli and Watts (2005) recommended more detailed and realistic simulations of deforming slides are carried out. The importance of realistic slide dynamics (i.e. acceleration and maximum velocity) and internal deformation during the wave-generating stage of slide motion motivates the choice of numerical modelling approach used in this work, which is described in the next section (3).

3. Methods

3.1. Fluidity: Governing Equations

Fluidity is a flexible finite-element/control-volume modelling framework, which allows for the numerical solution of several equation sets (Piggott et al., 2008). It has been used in a number of fluid flow studies, ranging from laboratory to ocean-scale (e.g. Wells et al., 2010; Hill et al., 2012; Hiester et al., 2011; Parkinson et al., 2014). In an ocean modelling context, Fluidity has been used to model both modern and ancient earthquake-generated tsunami (Oishi et al., 2013; Mitchell et al., 2010; Shaw et al., 2008), and tsunami generated by three-dimensional rigid-block submarine slides with prescribed motion, in a study of the ancient Storegga Slide (Hill et al., 2014).

Here, Fluidity is used to solve the single phase incompressible Navier-Stokes equations:

$$\rho\left(\frac{\partial \boldsymbol{u}}{\partial t} + \boldsymbol{u}\cdot\nabla\boldsymbol{u}\right) = -\nabla p + \left(\mu\nabla^2\boldsymbol{u}\right) - \rho g\boldsymbol{k}, \tag{1a}$$

$$\nabla\cdot\boldsymbol{u} = 0, \tag{1b}$$

where $\boldsymbol{u}$ is the velocity vector, t represents time, p is pressure, μ is the dynamic viscosity, ρ is the density, and for this work we assume that we are in a coordinate system where g, the gravitational acceleration, acts in the z direction: $\boldsymbol{k} = (0, 0, 1)^T$.

For incompressible flows with variable density, an additional equation is required to close the system; we refer to this as the equation of state. In the approaches used here, this equation relates the bulk density to the volume fractions of materials in the problem, or the concentration of sediment, along with the associated material properties. The equation of state will depend on the approach used with more details given in sections 3.1.1 and 3.1.2. Further details of the discretisation methods employed in this work are given in section 3.2.

3.1.1. SEDFS: Sediment, Water and Free Surface

The SEDFS approach uses a scalar tracer field describing the sediment concentration (particle volume fraction) to represent the dense slide. The sediment is of a user-defined density and sinking velocity (Parkinson et al., 2014). The user can add as many sediment tracer fields as required. Each sediment tracer field, indexed i, represents the concentration, c_i, of that sediment class, which behaves as any other tracer field, except that it can also be subject to a settling velocity, u_{si}. The scalar equation governing the evolution of the suspended sediment mass is:

$$\frac{\partial c_i}{\partial t} + \nabla \cdot c_i(\mathbf{u} - \boldsymbol{k} u_{si}) = \nabla \cdot (\overline{\overline{\kappa}} \nabla c_i). \tag{2}$$

The settling velocity, u_{si} is the *hindered sinking velocity*, which depends on the sediment concentration. Here, due to the high density of the slide, the sinking velocity is negligible and thus ignored. $\overline{\overline{\kappa}}$ is the diffusivity of the sediment and here is set to a small value, 10^{-6} m^{2}s^{-1}.

In this work we assume a single sediment class and denote its concentration of particles in the fluid c_s. The equation of state in this case takes the form

$$\rho = (1 - c_s)\rho_w + c_s \rho_s, \tag{3}$$

where ρ_s is the density of the individual sediment particles and ρ_w is the density of the water. In the laboratory scale test case presented here, ρ_s is 2650 kgm^{-3}, ρ_w is 1000 kgm^{-3} and the maximum value for c_s is 0.58, giving a slide bulk density of 1950 kgm^{-3} . (For the large scale test case the maximum value for c_s is the same, ρ_s is 2724 kgm^{-3} and the slide bulk density is 2000 kgm^{-3}.) Further details of this SEDFS approach may be found in (Parkinson et al., 2014). The approach is similar to that of Ma et al. (2013).

To simulate the evolution of the water surface in response to the slide dynamics in SEDFS, we use Fluidity's free-surface boundary condition option (Funke et al., 2011; Oishi et al., 2013). This moves the upper boundary of the computational domain, with a linear stretching of the nodes/elements in the interior of the domain down to the fixed position of the domain's lower boundary.

3.1.2. MM2FS: slide, water and free surface and MM3: slide, water and air

Here, two multi-material approaches are considered which differ in whether air is explicitly modelled or not, and hence whether the free surface method described above needs to be employed to simulate the evolution of the water surface. In these models, volume fraction fields, φ_i, are used to describe the location of different materials. Each of the n_φ volume fraction fields vary in $[0, 1]$ and should sum to unity everywhere:

$$\sum_{i=1}^{n_\varphi} \varphi_i = 1. \tag{4}$$

In this work, either two materials ($n_\varphi = 2$, MM2FS: slide and water), or three materials ($n_\varphi = 3$, MM3: slide, water and air), are modelled. MM2FS has many similarities to SEDFS, including the 'FS' free surface method presented above being used to represent the location of the upper boundary to the domain. The differences between MM2FS and SEDFS are described in more detail in section 3.2

Since, from (4), one of the volume fraction fields (here always water) can be recovered from the others using

$$\varphi_{n_\varphi} = 1 - \sum_{i=1}^{n_\varphi - 1} \varphi_i, \tag{5}$$

$n_\varphi - 1$ advection equations of the form

$$\frac{\partial \varphi_i}{\partial t} + \mathbf{u} \cdot \nabla \varphi_i = 0, \tag{6}$$

need to be solved. This implies only the slide volume fraction is solved for in the case of MM2FS, and the slide and air volume fractions are solved for in the case of MM3. In both approaches the location of the water is recovered using Equation (5).

In both MM2FS and MM3 the bulk density and viscosity used in Equation (1a) is recovered from the volume fraction weighted averages for all the materials in each approach using:

$$\rho = \sum_{i=1}^{n_\varphi} \varphi_i \rho_i, \qquad \mu = \sum_{i=1}^{n_\varphi} \varphi_i \mu_i, \tag{7}$$

where ρ_i and μ_i represent the constituent densities and viscosities of the individual materials.

For the laboratory scale test case, the densities of slide, water and air (if MM3) are 1950 kgm^{-3}, 1000 kgm^{-3} and 1 kgm^{-3} respectively. In the large scale test case the densities are the same except for the slide, which has a density of 2000 kgm^{-3}. In the MM3 approach the height of the air above the water is chosen to be several times the expected maximum wave height. Since the air is explicitly modelled in this approach, with the free surface being represented by the interface between water and air, this approach can naturally handle wave overturning/breaking. In the 'FS' approach, the inability to simulate wave breaking is a limitation.

3.2. Discretisation

Fluidity uses the finite element method to solve the Navier-Stokes equations. Several velocity-pressure representation choices (also known as element pairs) are available and vary depending on the approach employed (sections 3.1.1 and 3.1.2). A mixed discretisation approach can be taken where different function spaces are used to represent velocity and pressure. Implicit time-stepping (the theta method) is used and, following linearisation of the nonlinear advection terms, the associated linear solves for the discretised velocity and pressure systems are conducted in a segregated manner within a pressure-projection framework which enforces a divergence-free velocity field (Piggott et al., 2008). Following an update to velocity, scalar advection (-diffusion) equations for sediment concentration or material volume fractions are then solved using flux-limited control volume discretisation methods which feed into an updated density via the equation of state (3 or 7). Within a time step, two Picard iterations are then utilised to deal with nonlinearity and the coupling between all of the unknowns in the complete system. In addition, in the simulations presented here adaptive time-stepping is used, where the time-step varies, depending on a user-specified maximum Courant number.

For the SEDFS approach (section 3.1.1), (1a) and (1b) are discretised using a linear continuous Galerkin approximation (P1) choice for both velocity and pressure (Piggott et al., 2008). Within a theta time-stepping algorithm, $\theta = 0.5$ is selected yielding the second-order Crank-Nicolson method for velocity. To aid stability a streamline upwind method is used to treat the nonlinear advection term. Here the sediment concentration field(s), c_s, is discretised using a control volume method on the dual of the triangular finite element mesh, which is denoted here by P1CV. A flux-limited control volume method is used to solve this scalar equation (Wilson, 2009; Piggott et al., 2009). The Sweby flux limiter (Sweby, 1984) is used to ensure a bounded flux.

The MM2FS approach (section 3.1.2) has many similarities to the SEDFS approach, but with a different underlying finite element pair, and the use of a more compressive flux limiter (Leonard, 1991). Compared to the Sweby limiter, the more compressive limiter used in the the MM2FS approach enforces a much sharper interface between the slide and water, typically within one element width. For the discretisation of the equations for the volume fractions, (4) and (5) we again use a control volume method. A fully explicit first-order time-stepping scheme is used in combination with a 'sub-cycling' approach which ensures a maximum Courant number of 0.25 (Wilson, 2009). For the discretisation of the momentum and continuity equations, (1a) and (1b), a piecewise constant (P0) approximation is used for velocity. For MM3, pressure is discretised using the same approximation as the volume fraction fields, i.e. using the P1CV discretisation. The same pressure space is also used as the test space for the continuity equation (1b). The consistency with the volume fraction discretisation leads to a method that is both bounded and conservative (Wilson, 2009). For the MM2FS approach, a P1CV based method is not available for the combined pressure and free-surface field. In this case, we therefore combine the P0 velocity discretisation with a piecewise linear (P1) discretisation for pressure and free surface. As a result the volume fraction discretisation is not conservative. However, for the cases studied here the amount of conservation loss was negligible.

In MM3, the interface between water and slide is dealt with as for MM2FS. The interface between air and water is also handled using a compressive limiter, with a coupled approach ensuring that the limiter maintains boundedness for all volume fraction fields (Wilson, 2009).

Further details of the discretisation methods employed can be found in Piggott et al. (2008), Wilson (2009) and the Fluidity manual (AMCG, 2015).

3.3. Mesh Adaptivity

With the goal of maximising computational efficiency, here we investigate the utility of the dynamic mesh adaptivity algorithms available within Fluidity. Specifically, so-called mesh optimisation algorithms are considered that aim to periodically improve the mesh, through the minimisation of an optimisation functional, via a series of heuristic operations that locally update the shape, size or connectivity of the mesh.

The optimisation algorithm aims to achieve elements of given edge lengths, which can vary throughout the mesh. A measure of the size and shape of individual elements is provided by the optimisation functional, and these quantities are evaluated with respect to a metric tensor, M.

For a chosen field (in this work the volume fraction of water, φ_{water}) the metric, M is defined by:

$$M = \frac{1}{\varepsilon_{\varphi_{water}}} |H(\varphi_{water})|, \tag{8}$$

where $\varepsilon_{\varphi_{water}}$ is a constant user-defined weight for φ_{water}. Based on sensitivity studies, in this work φ_{water} alone was used to construct M, to ensure the interfaces between materials were well resolved. $|H_{\varphi_{water}}|$ is the Hessian matrix (of second-order derivatives) for φ_{water} where the absolute values of its eigenvalues have been taken (Hiester et al., 2011). $|H_{\varphi_{water}}|$ describes the curvature of the volume fraction field in the different coordinate directions, and is used to identify regions of the domain that warrant fine or coarse resolution in the vertical and/or horizontal direction (Pain et al., 2001). The M chosen thus encodes the desired mesh resolution, which can be highly anisotropic.

Since M is motivated by linear interpolation theory the result of the mesh optimisation operation described above is to place finer resolution in regions with high curvature in solution fields, and coarser resolution where the field varies linearly. In practice, M is limited in order to place restrictions on the maximum and minimum element size, maximum allowable aspect ratio, the spatial gradation of element edge length, and maximum number of elements permitted. For more details and examples of this approach see Piggott et al. (2008); Hiester et al. (2011, 2014); Hill et al. (2012) and Parkinson et al. (2014) and references therein.

3.3.1. Metric advection

The concept of metric advection is considered in some of the simulations presented here to reduce the frequency of adapting the mesh. Metric advection involves the advection of each component of the metric with the flow field and is described further in Hiester et al. (2011). The motivation for advecting the metric is to pre–empt where higher resolution is likely to be required in between times when the mesh is adapted. For example, so that the interface between materials, including the fast moving head of the slide, does not advect outside the region of enhanced resolution and therefore potentially be subject to excessive numerical diffusion. This results in higher resolution over a greater area, and therefore an increased number of nodes, however, in principle it allows the frequency of mesh adapts to be reduced whilst maintaining a good representation of the dynamics in the simulation.

3.3.2. Vertically aligned adaptivity

For relatively high aspect ratio problems it has been found that maintaining columns of elements in the vertical direction has advantages for stability. Fully unstructured meshes without any alignment in the vertical direction, can give rise to artificial horizontal gradients of fields that only vary vertically. For instance, in the MM3 approach, the initial air-water interface should be completely flat and remain at rest; however, with no vertical alignment of the nodes in the mesh, small artificial gradients in the hydrostatic pressure will initiate spurious waves leading to instability.

Despite the restriction to vertical columns of elements, adaptive resolution in both the horizontal and vertical direction can still be achieved using a two-stage approach. In the first stage, a horizontal surface mesh is created with varying resolution according to the horizontal components of the metric, M. In the second stage this mesh is extruded vertically by creating columns of nodes under each node of the horizontal mesh. The distance between the nodes (vertical resolution) can be chosen for each column independently. Finally the nodes are connected into cells.

Since the test cases considered here are only two-dimensional, both the horizontal mesh, and the vertical meshes (columns of nodes) below each surface node, are one-dimensional and mesh adaptivity is straight-forward. First we obtain the desired new edge lengths Δx_i by projecting the metric in the appropriate direction given by a unit vector $\hat{e}$, and using the following relation:

$$\Delta x_i^2 \; \hat{e}^T M_i \hat{e} = 1. \tag{9}$$

This expresses the fact that the optimal edge when measured with the metric should have length one.

Next, the old mesh co-ordinates are mapped $x \mapsto \tilde{x}$ from physical space to a so called metric space using:

$$\tilde{x}_1 = 0; \tilde{x}_i = \tilde{x}_{i-1} + \frac{x_i - x_{i-1}}{\Delta x_i}, \tag{10}$$

where Δx_i is the desired edge length between nodes x_i and x_{i-1}. Regions of the old mesh that require adaptation will give node spacings in metric space that differ from the ideal edge length of one. To define the new mesh, the first step is calculate the optimum number of nodes. Since the ideal edge length in metric space is one, this is simply $\tilde{x}_N$ rounded up to the nearest integer, where N is the last node of the old mesh. Then the new mesh is created using a uniform node separation of $\tilde{x}_N/\text{ceiling}(\tilde{x}_N)$, which is not quite equal to one but ensures an integer number of edges fit exactly into the domain. The final step is to map the position of the new nodes in metric space back to physical coordinates by interpolating from the old nodes in metric space.

If x'_j and $\tilde{x}'_j$ are the coordinates of the new mesh in physical and metric space, respectively, the interpolation is given by:

$$x'_j = \frac{\tilde{x}'_j - \tilde{x}_{i-1}}{\tilde{x}_i - \tilde{x}_{i-1}} x_i + \frac{\tilde{x}_i - \tilde{x}'_j}{\tilde{x}_i - \tilde{x}_{i-1}} x_{i-1} \tag{11}$$

for $\tilde{x}_{i-1} < \tilde{x}'_j < \tilde{x}_i$. This approach to one-dimensional mesh optimisation avoids directional bias and the need to crop the last element on one side of the domain.

4. Test cases

Two hypothetical submarine slide tsunami scenarios are considered, one at laboratory scale, validating against experimental data and benchmarking against prior numerical studies (Assier-Rzadkiewicz et al., 1997; Ma et al., 2013), and one at large scale, benchmarking against results from two different models in a scenario proposed by Horrillo et al. (2013) in the Gulf of Mexico.

4.1. Laboratory scale test case: Assier-Rzadkiewicz et al. (1997)

4.1.1. Problem set-up

This test case is taken from the laboratory experiments and numerical models of Assier-Rzadkiewicz et al. (1997), which itself is an extension using deformable slides, of the rigid block experiments and numerical models of Heinrich (1992). Heinrich (1992) used the two-dimensional incompressible Navier-Stokes equations, modelling water with a free surface, and the rigid slide with a moving bottom boundary. Assier-Rzadkiewicz et al. (1997) extended the NASA-VOF2D code to deformable slides, using a sediment-mixture numerical model. NASA-VOF2D solves the two-dimensional incompressible Navier-Stokes equations on a structured grid using low order finite differences and with a volume of fluid (VoF) approach to track the location of the free surface (Torrey et al., 1985), and treats the slide as a viscous fluid. Assier-Rzadkiewicz et al. (1997) also conducted laboratory experiments of granular slides in order to validate this model. The laboratory experiments used both solid (with 45° slope angle) and deformable slides (30° and 45° slopes angles). The deformable slides were represented using granular materials with three different grain size ranges. The tank used was 4 m long, 0.3 m wide and 2.0 m high, with a water depth of 1.6 m. The submarine slide mass was initially triangular in shape and spans the width of the channel, so this was considered a two-dimensional experiment. The dimensions of the slide were 0.65 m × 0.65 m, with a mean density of 1950 kgm^{-3}.

Ma et al. (2013) presented results of an extension of NHWAVE (Non-Hydrostatic WAVE model), which were also compared with Assier-Rzadkiewicz et al. (1997) (along with other scenarios). NHWAVE is a three-dimensional (non-hydrostatic) Navier-Stokes model using finite volume based discretisations on a structured grid which utilising free surface/bathymetry following σ coordinates and where the free surface movement is controlled through time-stepping the depth-integrated continuity equations (Ma et al., 2012). Similarly to NASA-VOF2D, the slide was represented using a sediment-mixture model. Assuming the same mean density as Assier-Rzadkiewicz et al. (1997), they use a volumetric sediment concentration of 0.58. They used a simplified slide model, which did not consider inter-granular stresses. A $\kappa - \varepsilon$ RANS turbulence model (Lin and Liu, 1998a,b; Ma et al., 2011, 2013) was used to calculate turbulent viscosity and diffusivity.

Here, Fluidity was used to simulate the same deformable slide scenario, from Assier-Rzadkiewicz et al. (1997). The initial condition is shown in Figure 1. Three approaches were compared within Fluidity: SEDFS, MM2FS and MM3. An adaptive timestep was used, with a requested maximum Courant number of 0.75. A free-slip, no-normal flow boundary condition was used on the slope and bottom of the tank. A dynamic water viscosity of 1 $\mathrm{kgm^{-1}s^{-1}}$ was used in all simulations, whilst dynamic viscosities of 10 $\mathrm{kgm^{-1}s^{-1}}$ and 0.1 $\mathrm{kgm^{-1}s^{-1}}$ were used for the slide and air respectively in MM2FS and MM3 simulations. Results are compared to the laboratory experiments and numerical results in Assier-Rzadkiewicz et al. (1997), as well as the numerical results from Ma et al. (2013), which used an approach similar to SEDFS.

4.1.2. Fixed mesh results

Results are presented for the same fixed mesh resolution as Assier-Rzadkiewicz et al. (1997) (0.1 m by 0.1 m element edge lengths) and at the same time levels. All three of the approaches available with Fluidity give similar results, and agree closely with the numerical results of Assier-Rzadkiewicz et al. (1997).

The slide geometry in the different models is very similar at both time intervals illustrated in Figure 2. The slide-water interface is most diffuse in SEDFS, owing to the less compressive advection scheme employed in this approach as well as the explicit inclusion of diffusion. Bulk densities at these time intervals are also shown in Assier-Rzadkiewicz et al. (1997) and Ma et al. (2013). In all cases the slide head overturns, and a second overturning billow of material separates off the main slide further up the slope.

Figure 3 (a,c) compares the surface wave forms predicted by Fluidity's three approaches. There is little difference between the three approaches at 0.4 seconds (a), because the slide has quickly accelerated into deep water, where any changes in the detailed slide geometry due to differences in the numerical treatment of the slide, have little influence on the wave produced.

Figure 3 (b,d) presents experimental results (Assier-Rzadkiewicz et al., 1997) along with previous numerical model results from NASA-VOF2D (Assier-Rzadkiewicz et al., 1997) and NHWAVE (Ma et al., 2013), for comparison with the range of results from the three different approaches in Fluidity. As observed with NASA-VOF2D (Assier-Rzadkiewicz et al., 1997) and NHWAVE (Ma et al., 2013), the maximum wave heights predicted by Fluidity are slightly greater than the experimental results. However, the amplitudes are lower than those obtained in the model used by Ma et al. (2013), and are also closer to the experimental results than NASA-VOF2D (Assier-Rzadkiewicz et al., 1997). At 0.8 seconds, for the wave trough located at 0.1 m, the Fluidity range matches very closely with the Ma et al. (2013) model, and for the wave trough located at 0.6 m, the Fluidity range matches well with the Assier-Rzadkiewicz et al. (1997) model. The peak in the wave train located at 0.1–0.5 m is higher in Fluidity than both Assier-Rzadkiewicz et al. (1997) and Ma et al. (2013), and is closer to that observed in the experiments. Ma et al. (2013) note that NHWAVE over-predicts the generated surface waves, because of faster movement of the slide in the simulation compared to the experiments. They attribute this to their simplified treatment of the slide, where stresses between sediment grains that would decelerate the slide, are not considered. However, SEDFS does not consider these stresses either, and the slide in SEDFS moves slower than the slide in NHWAVE, so it is unclear whether this simplification is the reason for the discrepancy, as SEDFS makes the same simplification.

In the results presented, a free-slip boundary condition was used, for consistency with the set-up used in Assier-Rzadkiewicz et al. (1997). However, a no-slip, or drag boundary condition may be more appropriate to reflect the friction of the slide along the slope at laboratory scale. Ma et al. (2013) appear to use a boundary condition with some drag, but this is not documented. The laboratory experiment was compared to two-dimensional numerical models, however, in reality the tank had some width and there would have been some friction between the water and the sides of the tank. This would have resulted in a reduction in wave height as energy was lost to friction. In all the models discussed here, this friction from the tank sides is not modelled or accounted for; accounting for it may improve the match between experimental and numerical results. On the other hand, some part of the discrepancy between models and experiment may be related to experimental limitations. For example, small-scale wave generation experiments can suffer from unavoidable scale effects not present in numerical models. For instance, surface tension at the air-water interface is a negligible force at large scales and hence neglected in numerical models, yet in small scale experiments this force may be an important component of wave resistance, providing additional dissipation. Given the possible experimental limitations, the comparisons with the numerical models NHWAVE and NASA-VOF2D are important for effective evaluation of Fluidity, and overall a good match is obtained between the three models.

For the models of Assier-Rzadkiewicz et al. (1997); Ma et al. (2013) results are not presented past 0.8 seconds. At this time the wave that propagates up-slope, in the opposite direction to the slide direction, steepens and starts to break. These models, and the models in Fluidity that employ a free surface boundary condition (MM2FS and SEDFS), are not able to model the wave breaking. However, the method used in MM3, tracks the interface between the air and water as a discontinuity in volume fraction, and is therefore able to continue simulating the wave evolution after breaking and back-fill occurs. This is shown in Figure 4.

A mesh sensitivity study (Figure 5) was undertaken to establish the optimum spatial resolution of the fixed meshes required to achieve a robust result (in terms of the wave amplitude and the location of the front of the slide).

These spatial resolution studies showed that cells with edge lengths of 0.01 m horizontally and vertically (leading to a mesh comprising 58,286 nodes) provided a good compromise between accuracy and efficiency. Increasing the resolution further had minimal effect on the maximum wave height, as shown in Figure 5. This was also the spatial resolution used by Assier-Rzadkiewicz et al. (1997). For fixed mesh simulations, run in serial, SEDFS took just over one hour to reach 0.8 seconds, the MM2FS set up took approximately 1.5 hours, MM3 set up took just over 2 hours.

4.1.3. Adaptive mesh results

For MM3 simulations, an adaptive mesh (e.g. Figure 6) was used to dynamically increase spatial resolution in regions of interest and decrease spatial resolution away from these regions. In the MM3 adaptive simulations described in Table 1, the mesh adapted to the volume fraction of water. This resulted in increased resolution at the boundaries between air-water, and water-slide. The spatial resolution decreases with increasing distance away from these boundaries. In a simulation it is possible to vary, amongst other options, the minimum and maximum edge length in both spatial dimensions; gradation factor (the factor by which the edge length can change from one element to the next); the field weight, $\varepsilon_{\varphi_{water}}$; whether metric advection is used or not; whether the mesh is adapted before the simulation begins; and how often the mesh is adapted. To determine the best adaptivity parameters, a suite of simulations were run. A sample of these simulations and their parameters are described in Table 1.

In Figure 5 the maximum wave height observed in each simulation is plotted for MM3 fixed mesh simulations (blue line), with edge lengths of

Simulation name	Minimum Edge Lengths: horizontal, vertical (m)	Maximum Edge Lengths: horizontal, vertical (m)	Metric Advection	No. of timesteps between mesh adapts
a1	0.01, 0.01	4, 0.5	on	20
a2	0.05, 0.05	4, 0.5	on	20
a3	0.01, 0.01	10, 5	on	20
a4	0.01, 0.01	4, 0.5	off	20
a5	0.01, 0.01	4, 0.5	on	10
a6	0.01, 0.01	1, 0.1	on	20

Table 1: Parameters for lab scale adaptive simulations

0.04, 0.02, 0.01, 0.005, and 0.0025 m. This shows the maximum wave heights at 0.4 seconds and 0.8 seconds, converge to approximately 3.3 cm and 6.3cm respectively. For the adaptive mesh simulations the maximum wave height is plotted against the average number of nodes employed during the simulation (between the first adapt of the mesh and when the simulation reached 0.8 seconds). The error bars displayed show the maximum and minimum number of nodes during the simulation.

A reduction in the maximum edge length permitted during the simulation (a6 from a1), results in a maximum wave height closer to the converged value and therefore increased accuracy. However, there is also an increase in computational cost, because the number of nodes increases. Compared to the fixed mesh simulation, simulation a6 used almost an order of magnitude fewer nodes to obtain the converged value for the wave height. An increase in the minimum edge length (a2 from a1) or maximum edge length (a3 from a1) permitted during the simulation leads to decrease in accuracy, and there is little, or no, saving in computational cost. This is because both these changes produce a mesh with less spatial variation in edge length. Metric advection predicts where higher spatial resolution will be needed in the future, and increases resolution accordingly. Therefore, not employing metric advection (a4 from a1) results in increased likelihood of the dynamics of interest (here, the interface between materials) propagating out of the regions of high resolution, and an associated decrease in accuracy.

Using meshes that adapt more frequently (a5 from a1) is also not advantageous as it is computationally more expensive and additional small errors are introduced during the interpolation of fields between the pre– and post–adapted meshes. These are usually insignificant but can accumulate if the mesh adapts too frequently.

The adaptive simulation a6, uses only 20% of the nodes used in the fixed mesh simulation that achieves the same result. Simulation a6 uses the same minimum edge length as the edge length in the fixed mesh, however the edge length is coarsened away from material interfaces, and this leads to a reduction in number of nodes and therefore lower computational expense. The simulation time is reduced from 120 minutes (fixed mesh MM3) to approximately 20 minutes (adaptive mesh MM3, simulation a6).

4.2. Large scale test case: Gulf of Mexico, Horrillo et al. (2013)

4.2.1. Problem set-up

To benchmark Fluidity for a full scale tsunamigenic submarine slide event, the recent simulations of Horrillo et al. (2013) were used. In this work they present TSUNAMI3D, their three-dimensional Navier-Stokes model for water and submarine slide, and validate it against the laboratory experiments of Liu et al. (2005), before applying it to a full-scale historical scenario in the Gulf of Mexico in two and three dimensions comparing TSUNAMI3D and a more diffusive commercial CFD program, FLOW3D.

TSUNAMI3D builds on the classical VoF formulation of Hirt and Nichols (1981) to track both the water surface and slide interface on a structured grid with a 3rd order finite difference scheme to solve the incompressible Navier-Stokes system. The VoF method determines regions containing water and slide material, with corresponding cell-weighted values of physical properties (density and viscosity) used in the momentum equation, in a very similar manner to the MM2FS and MM3 approaches employed in this work. TSUNAMI3D uses a simplified treatment of the free surface: the free surface in each column of cells is treated as horizontal, and consequently, wave breaking cannot be modelled. The water and slide are modelled as two incompressible, Newtonian fluids. For the full-scale tsunami simulations in a vertical two-dimensional slice domain (Horrillo et al., 2013) TSUNAMI3D is configured to only employ two cells in the "third" dimension.

In the two-dimensional full-scale scenario considered, the slide is on average approximately 150 m thick, 30 km long and the slope is approximately 1.6%. Their domain is 100 km across by 1.24 km high, with 496,000 cells, which are each 100 m across and 10 m high. The initial densities of the water and slide are 1000 kgm^{-3} and 2000 kgm^{-3} respectively. With bathymetry data and slide geometry provided by Horrillo (pers. comm) the two-dimensional simulation is replicated using Fluidity, with the same geometry and fluid densities. The set-up is shown in Figure 7. In Fluidity, the values for dynamic viscosity, in the horizontal and vertical respectively are set as 10^6 $kgm^{-1}s^{-1}$ and 10^3 $kgm^{-1}s^{-1}$ for water, and 10^7 $kgm^{-1}s^{-1}$ and 10^3 $kgm^{-1}s^{-1}$ for the slide. Viscosity values incorporate both the physical viscosity and the turbulent viscosity. These 'eddy' viscosity values were selected in order to dampen any instabilities at the interface between water and slide, whilst being low enough to have a negligible effect on the overall motion of the slide. The meshes used in this work employ elements with a high aspect ratio i.e. with a far larger element edge length in the horizontal direction than the vertical direction; anisotropic values for 'eddy' viscosity are often required for simulations on such meshes.

The problem was reproduced using the three available methods: SEDFS, MM2FS and MM3. An adaptive timestep was used, with a requested maximum Courant number of 0.5. A free-slip boundary condition on the water bottom was used.

4.2.2. Fixed mesh results

Density contour plots at three times in each simulation (3, 7 and 10 minutes) are shown in Figure 8. As in the laboratory scale simulations, SEDFS (a) has a more diffuse interface between the slide and water, this is also reflected in the water surface, resulting in a smooth free surface. In all three approaches material builds up in the slide head and the position of the slide head is almost identical. Consistent with Horrillo et al. (2013) and Løvholt et al. (2015), we also find that wave generation is largely controlled by the initial movement/acceleration of the slide under gravity, as opposed to the later deformation and run out of the slide in deeper water.

Water surface wave forms obtained by Fluidity at 3, 7 and 10 minutes using the three different approaches in Fluidity are compared in Figure 9 (a, c, e). Between the three approaches there is very good agreement in wave amplitudes and the locations of the wave minimums and maximums.

At 10 minutes, there is more variation in the three approaches (Figure 9e). This is due to the different behaviour of the slide in each case, the ability of the model to handle wave breaking, and the nature of the interface between materials, affecting the diffusion of the slide material into the water. The range of water surface elevations are compared to the two model results in Horrillo et al. (2013), TSUNAMI3D and FLOW3D, at the same time intervals (Figure 9b, d, f). Good agreement (within 10%) in wave amplitude and wave form is seen between the three models at all time levels. However, the forwarding propagating wave forms produced by Fluidity are consistently slightly ahead of the other models and has a higher maximum peak at 7 minutes (Figure 9d). The rearward propagating wave form produced by Fluidity tends to lie between the TSUNAMI3D and FLOW3D results.

4.2.3. Adaptive mesh results

In Figure 10 the maximum wave heights, at 3 minutes (a) and 7 minutes (b), are plotted against number of nodes for MM3 fixed mesh simulations (blue line), with edge lengths in the horizontal/vertical of: 400 $\times$ 40 m, 200 $\times$ 20 m, 100 $\times$ 10 m, 50 $\times$ 5 m, 20 $\times$ 2 m and 10 $\times$ 1 m. The maximum wave heights at 3 minutes and 7 minutes converge to approximately 16 m and 43 m respectively. Cells with edge lengths of 50 m in the horizontal and 5 m in the vertical provide a reasonable compromise between accuracy and computational expense.

An adaptive mesh (e.g., a section of which is shown in Figure 11) was used to increase spatial resolution at the interfaces between slide and water, and water and air. Coarser spatial resolution can be seen with increasing distance from these regions and despite the columnar restriction in vertically aligned adaptivity, the mesh resolution can be seen varying locally in both directions. In Figure 10 the maximum wave height for four adaptive mesh simulations are plotted against the average number of nodes during each simulation. Error bars show the maximum and minimum number of nodes between the first adapt and when the simulation reached 10 minutes.

Parameters for the four adaptive mesh simulations shown in Figure 10 are described in Table 2. The adaptivity settings were varied to establish the optimum values. Increasing maximum horizontal edge length (h2 from h1) resulted in only a slight deterioration in the solution accuracy and significantly reduces the minimum and maximum number of nodes in the simulation. However, as the average number of nodes is relatively unchanged relative to h1, it does not constitute a substantial improvement. Increasing minimum vertical edge length (h3 from h1), reduced the maximum and average number of nodes in simulation, however, this computational saving comes with substantial loss in accuracy. The absence of metric advection (h4 from h1) resulted in increased likelihood of the material interfaces propagating out of the regions of high resolution, causing material to diffuse further into the water column, disturbing the water surface, and resulting in decreased accuracy. The effects of adaptivity parameters observed in the large scale test case are consistent with the effects observed in the laboratory scale case.

Adaptive simulation h1 uses, on average, an order of magnitude fewer nodes than the number of nodes needed in a fixed mesh simulation to obtain a very similar result. Using a minimum element edge length of 100×2 m, and maximum element edge length of 200×200 m, the simulation time, in serial, is reduced to approximately 4 hours, compared to 10 hours for a fixed

Simulation name	Minimum Edge Length: vertical (m)	Minimum Edge Length: horizontal (m)	Maximum Edge Length: vertical (m)	Maximum Edge Length: horizontal (m)	Metric Advection	No. of timesteps between mesh adapts
h1	2	100	200	100	on	20
h2	2	100	200	400	on	20
h3	10	100	200	100	on	20
h4	2	100	200	100	off	20

Table 2: Parameters for large scale adaptive simulations

mesh resolution of 100 × 10 m. The adaptive results shown are all within 10% of the converged answer at each time. This indicates that the result is not greatly dependant on the adaptivity parameters that are chosen.

5. Discussion

The three modelling approaches considered in this work have differing computational costs. SEDFS is the most efficient, followed by MM2FS, then MM3. This is largely governed by the increasing number of fields that are solved for (volume fractions or concentrations) and the need to sub-cycle the solution for the volume fraction. However, there is also an increase in the number of degrees of freedom from SEDFS to MM2FS to MM3. This is due to the changes in discretisation methods employed, as well as MM3 representing the additional volume of air above the water surface.

As submarine slides are often subcritical – the wave speed is far greater than the speed of the slide – the initial slide movement dominates the wave generation (Harbitz et al., 2014; Løvholt et al., 2015). This is typically seen in the simulations presented here, where the waveform is largely determined by the initial acceleration of the slide, when it is at relatively shallow depths, and not by later details of the slide movement and deformation. The three different approaches produce very similar waveforms and the slides evolve similarly in each case.

Each of the three approaches used in this work have advantages justifying their use for different scenarios. In the high slide density scenarios considered here, the SEDFS approach differs from MM2FS and MM3 in how the concentration/volume fraction is advected i.e the choice of flux limiter (see section 3.2); using SEDFS there is greater diffusion of the slide material. In submarine slide scenarios with lower particle concentrations, where the settling velocity is non-negligible, SEDFS allows other aspects of slide dynamics to be considered, including material deposition from the slide (providing a method to compare to deposits) and its transformation from submarine slide into turbidity current. However, the full model including sediment settling dynamics is only valid for dilute sediment concentrations. More dilute flows will favour the more diffusive SEDFS approach and so the most appropriate choice of model will also depend on the sediment concentration. Another advantage of this approach is that, the free surface method (used in SEDFS and MM2FS) has the potential to facilitate more straightforward coupling to a basin scale wave propagation model in the future, or between different approaches within Fluidity.

A disadvantage of SEDFS is that it does not allow the slide and water to have different viscosities; however, this flexibility is available in MM2FS and MM3. Both MM2FS and MM3 allow modelling of a sharp interface between materials, whereas SEDFS assumes a more diffusive interface. MM3 is more flexible, as it has the advantage of being able to model wave breaking during the generation phase. However, in realistic submarine slide scenarios wave breaking does not often occur because submarine slides are subcritical and often initiate in deep water, implying that wave amplitudes are typically low relative to wavelength. If wave breaking does not occur, modelling the third material (air) is an unnecessary expense, because the computational domain is larger, and it requires high mesh resolutions at the water–air interface. In this case, simulations that employ Fluidity's free-surface method (MM2FS, SEDFS) are computationally more efficient. Additionally, MM3 requires higher spatial resolution before convergence of the maximum wave height is reached (comparison not shown). This may be a consequence of how water surface elevation is extracted from MM3 simulations, as the interface position is not calculated explicitly as it is with the method used in MM2FS and SEDFS. Instead, the air–water interface position is calculated based on the air and water volume fractions, and hence depends more sensitively on spatial resolution.

6. Conclusions

Fluidity has been successfully compared to laboratory experiments and four other numerical models (two at laboratory scale and two using a full scale slide). Three different approaches (SEDFS, MM2FS and MM3) within Fluidity have been successfully applied to dynamically model submarine slide evolution at both laboratory and large scales using fixed meshes. Each approach has advantages and disadvantages, so future use will depend on each specific application. Mesh adaptivity has also been applied at both laboratory and realistic scales, tracking important features of the slide geometry as the simulation progresses. The importance of slide geometry, deformation and dynamics will be the subject of future work. Mesh adaptivity has been shown to reduce the computational expense of simulations, whilst maintaining accuracy. At both scales we were able to reduce the number of nodes by at least an order of magnitude. This can be utilised in the future to simulate scenarios previously considered too computationally expensive, for example in three-dimensional simulations.

7. Acknowledgements

The authors are grateful to Juan Horrillo for kindly providing set-up files for the Gulf of Mexico example. We would like to thank Carl Harbitz and an anonymous reviewer for very helpful reviews that improved this manuscript. JH, GC and MDP acknowledge funding from NERC under project (NE/K000047/1). The authors would like to acknowledge the use of the Imperial College London HPC service.

8. References

Abadie, S., Morichon, D., Grilli, S., Glockner, S., Sep. 2010. Numerical Simulation of Waves Generated by Landslides using a Multiple-Fluid Navier–Stokes Model. Coastal Engineering 57 (9), 779–794. URL http://linkinghub.elsevier.com/retrieve/pii/S0378383910000396

Abadie, S. M., Harris, J. C., Grilli, S. T., Fabre, R., May 2012. Numerical Modeling of Tsunami Waves Generated by the Flank Collapse of the Cumbre Vieja Volcano (La Palma, Canary Islands): Tsunami Source and Near Field Effects. Journal of Geophysical Research 117 (C5). URL http://www.agu.org/pubs/crossref/2012/2011JC007646.shtml

AMCG, Apr. 2015. Fluidity manual v4.1.11, Imperial College London.

Assier-Rzadkiewicz, S., Heinrich, P., Abatier, P. C. S., Avoye, B. S., 2000. Numerical Modelling of a Landslide-Generated Tsunami : The 1979 Nice Event. Pure and Applied Geophysics 157, 1707–1727.

Assier-Rzadkiewicz, S., Mariotti, C., Heinrich, P., 1997. Numerical Simulation of Submarine Landslides and their Hydraulic Effects. Journal of Waterway, Port, Coastal, and Ocean Engineering (August), 149–157.
URL http://ascelibrary.org/doi/abs/10.1061/(ASCE)0733-950X(1997)123:4(149)

Ataie-Ashtiani, B., Najafi-Jilani, A., Dec. 2008. Laboratory Investigations on Impulsive Waves caused by Underwater Landslide. Coastal Engineering 55 (12), 989–1004.
URL http://linkinghub.elsevier.com/retrieve/pii/S0378383908000586

Behrens, J., 2014. Towards real-time tsunami forecasting with efficient adaptive mesh methods and computing on demand strategies. In: 20th International Conference on Computational Methods in Water Resources. p. 7.

Berndt, C., Brune, S., Nisbet, E., Zschau, J., Sobolev, S. V., Apr. 2009. Tsunami Modeling of a Submarine Landslide in the Fram Strait. Geochemistry Geophysics Geosystems 10 (4).
URL http://www.agu.org/pubs/crossref/2009/2008GC002292.shtml

Bondevik, S., Løvholt, F., Harbitz, C., Mangerud, J., Dawson, A., Inge Svendsen, J., Jan. 2005a. The Storegga Slide Tsunami–Comparing Field Observations with Numerical Simulations. Marine and Petroleum Geology 22 (1-2), 195–208.
URL http://linkinghub.elsevier.com/retrieve/pii/S0264817204001904

Bondevik, S., Mangerud, J., Dawson, S., Dawson, A., Lohne, Ø., Aug. 2005b. Evidence for Three North Sea Tsunamis at the Shetland Islands Between 8000 and 1500 Years Ago. Quaternary Science Reviews 24 (1415), 1757–1775.
URL http://www.sciencedirect.com/science/article/pii/S0277379105000739

Breien, H., De Blasio, F. V., Elverhøi, A., Nystuen, J. P., Harbitz, C. B., Nov. 2010. Transport Mechanisms of Sand in Deep-Marine Environments–Insights Based on Laboratory Experiments. Journal of Sedimentary Research 80 (11), 975–990.
URL http://jsedres.sepmonline.org/cgi/doi/10.2110/jsr.2010.079

Bugge, T., Belderson, R., Kenyon, N., 1988. The Storegga Slide. Philosophical Transactions of the Royal Society London 325 (1586), 357–388.
URL http://www.jstor.org/stable/10.2307/38068

Dan, G., Sultan, N., Savoye, B., Nov. 2007. The 1979 Nice harbour catastrophe revisited: Trigger mechanism inferred from geotechnical measurements and numerical modelling. Marine Geology 245 (1-4),

40–64.
URL http://linkinghub.elsevier.com/retrieve/pii/S0025322707001545

Dawson, A., Long, D., Smith, D., Aug. 1988. The Storegga Slides: Evidence from eastern Scotland for a Possible Tsunami. Marine Geology 82 (34), 271–276.
URL http://www.sciencedirect.com/science/article/pii/0025322788901466

Elverhøi, A., Breien, H., Blasio, F. V., Harbitz, C. B., Pagliardi, M., Jul. 2010. Submarine landslides and the importance of the initial sediment composition for run-out length and final deposit. Ocean Dynamics 60 (4), 1027–1046.
URL http://link.springer.com/10.1007/s10236-010-0317-z

Elverhøi, A., Issler, D., De Blasio, F. V., Ilstad, T., Harbitz, C. B., Gauer, P., 2005. Emerging insights into the dynamics of submarine debris flows. Natural Hazards and Earth System Science 5 (5), 633–648.
URL http://hal.archives-ouvertes.fr/hal-00299250/

Enet, F., Grilli, S., 2005. Tsunami Landslide Generation: Modelling and Experiments. In: Ocean Waves Measurement and Analysis, 5th International Symposium.

Enet, F., Grilli, S., 2007. Experimental Study of Tsunami Generation by Three-dimensional Rigid Underwater Landslides. Journal of Waterway, Port, Coastal and Ocean Engineering (December), 442–454.
URL http://ascelibrary.org/doi/pdf/10.1061/(ASCE)0733-950X(2007)1333A6(442)

Enet, F., Grilli, S., Watts, P., 2003. Laboratory Experiments for Tsunami Generated by Underwater Landslides: Comparison with Numerical Modeling. In: Proceedings of The Thirteenth (2003) International Offshore and Polar Engineering Conference. Vol. 5. pp. 372–379.
URL http://e-book.lib.sjtu.edu.cn/isope2003/pdffiles/volume3/3056p372.pdf

Fine, I., Rabinovich, A., Bornhold, B., Thomson, R., Kulikov, E., Feb. 2005. The Grand Banks Landslide-Generated Tsunami of November 18, 1929: Preliminary Analysis and Numerical Modeling. Marine Geology 215 (1-2), 45–57.
URL http://linkinghub.elsevier.com/retrieve/pii/S002532270400324X

Fine, I., Rabinovich, A., Kulikov, E., Thomson, R., Bornhold, B., 1998. Numerical Modelling of Landslide-generated Tsunamis with Application to the Skagway Harbor Tsunami of November 3, 1994. In: Proc. Int. Conf. on Tsunamis, Paris. pp. 211–223.

Fuhrman, D. R., Madsen, P. A., Jul. 2009. Tsunami Generation, Propagation, and Run-up with a high-order Boussinesq Model. Coastal Engineering 56 (7), 747–758.
URL http://www.sciencedirect.com/science/article/pii/S0378383909000349

Funke, S. W., Pain, C. C., Kramer, S. C., Piggott, M. D., Nov. 2011. A wetting and drying algorithm with a combined pressure/free-surface formulation for non-hydrostatic models. Advances in Water Resources 34 (11), 1483–1495.
URL http://www.sciencedirect.com/science/article/pii/S0309170811001564

Gauer, P., Elverhøi, A., Blasio, F. D., 2006. On Numerical Simulations of Subaqueous Slides: Backcalculations of Laboratory Experiments. Norwegian Journal of Geology, 295–300.

Gauer, P., Kvalstad, T. J., Forsberg, C. F., Bryn, P., Berg, K., Jan. 2005. The Last Phase of the Storegga Slide: Simulation of Retrogressive Slide Dynamics and Comparison with Slide-Scar Morphology. Marine and Petroleum Geology 22 (1-2), 171–178.
URL http://linkinghub.elsevier.com/retrieve/pii/S0264817204001874

Glimsdal, S., Pedersen, G. K., Harbitz, C. B., Løvholt, F., Jun. 2013. Dispersion of tsunamis: does it really matter? Nat. Hazards Earth Syst. Sci. 13 (6), 1507–1526.
URL http://www.nat-hazards-earth-syst-sci.net/13/1507/2013/

Grilli, S., Watts, P., 2005. Tsunami Generation by Submarine Mass Failure. I: Modeling, Experimental Validation, and Sensitivity Analyses. Journal of Waterway, Port, Coastal, and Ocean Engineering 131, 283–297.

Haflidason, H., Lien, R., Sejrup, H. P., Forsberg, C. F., Bryn, P., Jan. 2005. The Dating and Morphometry of the Storegga Slide. Marine and Petroleum Geology 22 (12), 123–136.
URL http://www.sciencedirect.com/science/article/pii/S0264817204001837

Haflidason, H., Sejrup, H. P., Nygrd, A., Mienert, J., Bryn, P., Lien, R., Forsberg, C. F., Berg, K., Masson, D., Dec. 2004. The Storegga Slide: Architecture, Geometry and Slide Development. Marine Geology 213 (14), 201–234.
URL http://www.sciencedirect.com/science/article/pii/S0025322704002713

Harbitz, C. B., 1992. Model Simulations of Tsunamis Generated by the Storegga Slides. Marine Geology 105 (1), 121.
URL http://www.sciencedirect.com/science/article/pii/002532279290178K

Harbitz, C. B., Løvholt, F., Pedersen, G., Masson, D. G., 2006. Mechanisms of Tsunami Generation by Submarine Landslides: A Short Review. Norsk Geologisk Tidsskrift 86 (3), 255.

Harbitz, C. B., Lvholt, F., Bungum, H., Jul. 2014. Submarine landslide tsunamis: how extreme and how likely? Natural Hazards 72 (3), 1341–1374.
URL http://link.springer.com/10.1007/s11069-013-0681-3

Heinrich, P., 1992. Nonlinear Water Waves Generated by Submarine and Aerial Landslides. Journal of Waterway, Port, Coastal, and Ocean Engineering 118 (3), 249–266.

Hiester, H., Piggott, M., Farrell, P., Allison, P., 2014. Assessment of spurious mixing in adaptive mesh simulations of the two-dimensional lock-exchange . Ocean Modelling 73 (0), 30–44.
URL http://www.sciencedirect.com/science/article/pii/S1463500313001844

Hiester, H. R., Piggott, M. D., Allison, P. A., 2011. The Impact of Mesh Adaptivity on the Gravity Current Front Speed in a Two-Dimensional Lock-Exchange. Ocean Modelling 38 (12), 1–21.
URL http://www.sciencedirect.com/science/article/pii/S1463500311000060

Hill, J., Collins, G. S., Avdis, A., Kramer, S. C., Piggott, M. D., 2014. How does multiscale modelling and inclusion of realistic palaeobathymetry affect numerical simulation of the storegga slide tsunami? Ocean Modelling.
URL http://www.sciencedirect.com/science/article/pii/S1463500314001164

Hill, J., Piggott, M. D., Ham, D. A., Popova, E. E., Srokosz, M. A., Oct. 2012. On the performance of a generic length scale turbulence model within an adaptive finite element ocean model. Ocean Modelling 56, 1–15.
URL http://www.sciencedirect.com/science/article/pii/S1463500312001023

Hirt, C. W., Nichols, B. D., Jan. 1981. Volume of fluid (VOF) method for the dynamics of free boundaries. Journal of Computational Physics 39 (1), 201–225.
URL http://www.sciencedirect.com/science/article/pii/0021999181901455

Horrillo, J., Wood, A., Kim, G.-B., Parambath, A., Dec. 2013. A Simplified 3-D Navier-Stokes Numerical Model for Landslide-Tsunami: Application to the Gulf of Mexico. Journal of Geophysical Research: Oceans 118 (12), 6934–6950.
URL http://onlinelibrary.wiley.com/doi/10.1002/2012JC008689/abstract

Jiang, L., LeBlond, P., Aug. 1992. The Coupling of A Submarine Slide and The Surface Waves Which It Generates. Journal of Geophysical Research 97 (C8), 12,731–12,744.

Jiang, L., LeBlond, P., 1993. Numerical Modeling of an Underwater Bingham Plastic Mudslide and the Waves Which it Generates. Journal of Geophysical Research 98 (93), 303–317.
URL http://www.agu.org/pubs/crossref/1993/93JC00393.shtml

Jiang, L., LeBlond, P. H., 1994. Three-Dimensional Modeling of Tsunami Generation Due to a Submarine Mudslide. American Meteorological Society 24, 559–572.

Kawata, Y., Benson, B. C., Borrero, J. C., Borrero, J. L., Davies, H. L., de Lange, W. P., Imamura, F., Letz, H., Nott, J., Synolakis, C. E., Mar. 1999. Tsunami in Papua New Guinea was as intense as first thought. Eos, Transactions American Geophysical Union 80 (9), 101–105.
URL http://onlinelibrary.wiley.com/doi/10.1029/99EO00065/abstract

Leonard, B. P., Jun. 1991. The ULTIMATE conservative difference scheme applied to unsteady one-dimensional advection. Comput. Methods Appl. Mech. Eng. 88 (1), 17–74.
URL http://dx.doi.org/10.1016/0045-7825(91)90232-U

LeVeque, R. J., George, D. L., Sep. 2008. High-Resolution Finite Volume Methods For The Shallow Water Equations With Bathymetry And Dry States. In: Advanced Numerical Models for Simulating Tsunami Waves and Runup. Vol. 10. World Scientific, pp. 43–73.

Lin, P., Liu, P. L.-F., Mar. 1998a. A numerical study of breaking waves in the surf zone. Journal of Fluid Mechanics 359, 239–264.

Lin, P., Liu, P. L.-F., Jul. 1998b. Turbulence transport, vorticity dynamics, and solute mixing under plunging breaking waves in surf zone. Journal of Geophysical Research: Oceans 103 (C8), 15677–15694.
URL http://onlinelibrary.wiley.com/doi/10.1029/98JC01360/abstract

Liu, P. L.-F., Wu, T.-R., Raichlen, F., Synolakis, C. E., Borrero, J. C., Jul. 2005. Runup and Rundown Generated by Three-Dimensional Sliding Masses. Journal of Fluid Mechanics 536, 107–144.

Løvholt, F., Pedersen, G., Gisler, G., Sep. 2008. Oceanic Propagation of a Potential Tsunami from the La Palma Island. Journal of Geophysical Research 113 (C9).
URL http://www.agu.org/pubs/crossref/2008/2007JC004603.shtml

Løvholt, F., Pedersen, G., Harbitz, C. B., Glimsdal, S., Kim, J., Oct. 2015. On the characteristics of landslide tsunamis. Phil. Trans. R. Soc. A 373 (2053), 20140376.
URL http://rsta.royalsocietypublishing.org/content/373/2053/20140376

Lynett, P. J., Borrero, J. C., Liu, P. L.-F., Synolakis, C. E., 2003. Field Survey and Numerical Simulations: A Review of the 1998 Papua New Guinea Tsunami. In: Bardet, J.-P., Imamura, F., Synolakis, C. E., Okal, E. A., Davies, H. L. (Eds.), Landslide Tsunamis: Recent Findings and Research Directions. Pageoph Topical Volumes. Birkhuser Basel, pp. 2119–2146, dOI: 10.1007/978-3-0348-7995-8_16.

Ma, G., Kirby, J. T., Shi, F., Sep. 2013. Numerical Simulation of Tsunami Waves Generated by Deformable Submarine Landslides. Ocean Modelling 69, 146–165.
URL http://www.sciencedirect.com/science/article/pii/S1463500313001170

Ma, G., Shi, F., Kirby, J. T., May 2011. A polydisperse two-fluid model for surf zone bubble simulation. Journal of Geophysical Research: Oceans 116 (C5), C05010.
URL http://onlinelibrary.wiley.com/doi/10.1029/2010JC006667/abstract

Ma, G., Shi, F., Kirby, J. T., 2012. Shock-capturing non-hydrostatic model for fully dispersive surface wave processes. Ocean Modelling 4344, 22–35.
URL http://www.sciencedirect.com/science/article/pii/S1463500311001892

Masson, D. G., Harbitz, C. B., Wynn, R. B., Pedersen, G., Løvholt, F., 2006. Submarine Landslides: Processes, Triggers and Hazard Prediction. Philosophical Transactions of the Royal Society A: Mathematical, Physical and Engineering Sciences 364 (1845), 2009–2039.

Mitchell, A. J., Allison, P. A., Piggott, M. D., Gorman, G. J., Pain, C. C., Hampson, G. J., 2010. Numerical Modelling of Tsunami Propagation with Implications for Sedimentation in Ancient Epicontinental Seas: The Lower Jurassic Laurasian Seaway. Sedimentology 228 (3), 8197.
URL http://www.sciencedirect.com/science/article/pii/S0037073810000692

Morichon, D., Abadie, S., Mar. 2010. Vague générée par un glissement de terrain influence de la forme initiale et de la déformabilité du glissement. La Houille Blanche (1), 111–117.
URL http://www.shf-lhb.org/10.1051/lhb/2010013

Nicolsky, D. J., Suleimani, E. N., Hansen, R. A., Dec. 2010. Numerical Modeling of the 1964 Alaska Tsunami in Western Passage Canal and Whittier, Alaska. Natural Hazards and Earth System Science 10 (12), 2489–2505.
URL http://www.nat-hazards-earth-syst-sci.net/10/2489/2010/

Oishi, Y., Piggott, M. D., Maeda, T., Kramer, S. C., Collins, G. S., Tsushima, H., Furumura, T., 2013. Three-dimensional tsunami propagation simulations using an unstructured mesh finite element model. Journal of Geophysical Research: Solid Earth 118 (6), 2998–3018.
URL http://dx.doi.org/10.1002/jgrb.50225

Pain, C. C., Umpleby, A. P., de Oliveira, C. R. E., Goddard, A. J. H., Apr. 2001. Tetrahedral mesh optimisation and adaptivity for steady-state and transient finite element calculations. Computer Methods in Applied Mechanics and Engineering 190 (2930), 3771–3796.
URL http://www.sciencedirect.com/science/article/pii/S0045782500002942

Parkinson, S. D., Hill, J., Piggott, M. D., Allison, P. A., Sep. 2014. Direct numerical simulations of particle-laden density currents with adaptive, discontinuous finite elements. Geosci. Model Dev. 7 (5), 1945–1960.
URL http://www.geosci-model-dev.net/7/1945/2014/

Piggott, M. D., Farrell, P. E., Wilson, C. R., Gorman, G. J., Pain, C. C., 2009. Anisotropic mesh adaptivity for multi-scale ocean modelling. Philosophical Transactions of the Royal Society of London A: Mathematical, Physical and Engineering Sciences 367 (1907), 4591–4611.

Piggott, M. D., Gorman, G. J., Pain, C. C., Allison, P. A., Candy, A. S., Martin, B. T., Wells, M. R., 2008. A New Computational Framework for Multi-Scale Ocean Modelling based on Adapting Unstructured Meshes. International Journal for Numerical Methods in Fluids 56 (8), 10031015.
URL http://onlinelibrary.wiley.com/doi/10.1002/fld.1663/abstract

Shaw, B., Ambraseys, N. N., England, P. C., Floyd, M. A., Gorman, G. J., Higham, T. F. G., Jackson, J. A., Nocquet, J.-M., Pain, C. C., Piggott, M. D., Apr. 2008. Eastern Mediterranean Tectonics and Tsunami Hazard Inferred from the AD 365 Earthquake. Nature Geosci 1 (4), 268–276.
URL http://dx.doi.org/10.1038/ngeo151

Smith, D., Shi, S., Cullingford, R., Dawson, A., Dawson, S., Firth, C., Foster, I., Fretwell, P., Haggart, B., Holloway, L., Long, D., Dec. 2004. The Holocene Storegga Slide Tsunami in the United Kingdom. Quaternary Science Reviews 23 (2324), 2291–2321.
URL http://www.sciencedirect.com/science/article/pii/S0277379104001003

Sue, L. P., Nokes, R. I., Davidson, M. J., Jan. 2011. Tsunami Generation by Submarine Landslides: Comparison of Physical and Numerical Models. Environmental Fluid Mechanics 11 (2), 133–165.
URL http://www.springerlink.com/index/10.1007/s10652-010-9205-9

Sue, L. P., Nokes, R. I., Walters, R. A., 2006. Experimental Modelling of Tsunami Generated by Underwater Landslides. Science of Tsunami Hazards.
URL http://ir.canterbury.ac.nz/handle/10092/50

Suleimani, E., Hansen, R., Haeussler, P. J., Feb. 2009. Numerical Study of Tsunami Generated by Multiple Submarine Slope Failures in Resurrection Bay, Alaska, during the MW 9.2 1964 Earthquake. Pure and Applied Geophysics 166 (1-2), 131–152.
URL http://www.springerlink.com/index/10.1007/s00024-004-0430-3

Sweby, P. K., 1984. High Resolution Schemes Using Flux Limiters for Hyperbolic Conservation Laws. SIAM Journal on Numerical Analysis 21 (5), 995–1011.
URL http://dx.doi.org/10.1137/0721062

Synolakis, C. E., Bardet, J.-P., Borrero, J. C., Davies, H. L., Okal, E. A., Silver, E. A., Sweet, S., Tappin, D. R., Apr. 2002. The Slump Origin of the 1998 Papua New Guinea Tsunami. Proceedings of the Royal Society A: Mathematical, Physical and Engineering Sciences 458 (2020), 763–789.
URL http://rspa.royalsocietypublishing.org/cgi/doi/10.1098/rspa.2001.0915

Tappin, D., Watts, P., Grilli, S. T., 2008. The Papua New Guinea Tsunami of 17 July 1998: Anatomy of a Catastrophic Event. Natural hazards and earth system sciences 8, 243266.
URL http://nora.nerc.ac.uk/6776/

Tappin, D. R., Apr. 2010. Submarine Mass Failures as Tsunami Sources: Their Climate Control. Philosophical Transactions of the Royal Society A: Mathematical, Physical and Engineering Sciences 368 (1919), 2417–2434.
URL http://rsta.royalsocietypublishing.org/cgi/doi/10.1098/rsta.2010.0079

Thomson, R. E., Rabinovich, A. B., Kulikov, E. A., Fine, I., Bornhold, B., 2001. On Numerical Simulation of the Landslide-Generated Tsunami of November 3, 1994 in Skagway Harbor, Alaska. In: Hebenstreit, G. (Ed.), Tsunami Research at the End of a Critical Decade. Vol. 18 of Advances in Natural and Technological Hazards Research. Springer Netherlands, pp. 243–282.

Torrey, M. D., Cloutman, L. D., Mjolsness, R. C., Hirt, C. W., Dec. 1985. Nasa-Vof2d: A Computer Program for Incompressible Flows with Free Surfaces. Tech. Rep. LA-10612-MS, Los Alamos National Lab., NM (USA).
URL http://www.osti.gov/scitech/biblio/5934123

Wagner, B., Bennike, O., Klug, M., Cremer, H., 2007. First Indication of Storegga Tsunami Deposits from East Greenland. Journal of Quaternary Science 22 (4), 321325.
URL http://onlinelibrary.wiley.com/doi/10.1002/jqs.1064/abstract

Watts, P., 1997. Water Waves Generated by Underwater Landslides. Ph.D. thesis, California Institute of Technology.

Watts, P., 1998. Wavemaker Curves for Tsunamis Generated by Underwater Landslides. Journal of waterway, port, coastal, and ocean engineering 124 (3), 127137.

Watts, P., 2000. Tsunami Features of Solid Block Underwater Landslides. Journal of Waterway, Port, Coastal, and Ocean Engineering 126 (3), 144–152.

Watts, P., Grilli, S., 2003. Underwater Landslide Shape, Motion, Deformation, and Tsunami Generation. In: Proceedings of the 13th Offshore and Polar Engingeering Conference. Vol. 5. pp. 364–371.

Watts, P., Imamura, F., Grilli, S., 2000. Comparing Model Simulations of Three Benchmark Tsunami Generation Cases. Science of Tsunami Hazards, 1–17.

Wells, M. R., Allison, P. A., Piggott, M. D., Hampson, G. J., Pain, C. C., Gorman, G. J., Jan. 2010. Tidal modeling of an ancient tide-dominated seaway, part 1: Model validation and application to global early cretaceous (aptian) tides. Journal of Sedimentary Research 80 (5), 393–410.
URL http://jsedres.geoscienceworld.org/content/80/5/393

Whittaker, C. N., Nokes, R. I., Davidson, M., 2012. Experimental and Numerical Modelling of Landslide-Generated Tsunamis. In: 18th Australasian Fluid Mechanics Conference.

Wilson, C., 2009. Modelling multiple-material flows on adaptive unstructured meshes. Ph.D. thesis, Imperial College London.

Yuk, D., Yim, S., Liu, P., Aug. 2006. Numerical Modeling of Submarine Mass-Movement Generated Waves Using RANS Model. Computers & Geosciences 32 (7), 927–935.
URL http://linkinghub.elsevier.com/retrieve/pii/S0098300405002682

9. Figure Captions

Figure 1: Geometry and initial condition for laboratory scale simulations, after Assier-Rzadkiewicz et al. (1997).

Figure 2: Density plots at t = 0.4 seconds and t = 0.8 seconds for initial water density 1000 kgm^{-3}, slide density 1950 kgm^{-3} in SEDFS (top), MM2FS (middle) and MM3 (bottom).

Figure 3: A comparison of water surface elevations for: (a,c) three different approaches by Fluidity: SEDFS (solid red), MM2FS (blue dotted) and MM3 (solid green) and (b,d) the spread in the results by Fluidity (yellow area bounded by black line) and the experimental results (red dotted) and NASA-VOF2D numerical results from (Assier-Rzadkiewicz et al., 1997) (purple) and NHWAVE (Ma et al., 2013) (solid blue) at t = 0.4 s (a,b) and t = 0.8 s (c,d).

Figure 4: Density plots with close-ups showing complex wave interactions, including wave breaking and back-fill in MM3 simulation at (a) 0.7 (b) 0.8 (c) 0.9 and (d) 1.0 seconds.

Figure 5: Maximum water surface elevations at 0.4 seconds (a) and 0.8 seconds (b) for MM3 simulations. Fixed mesh results for element edge lengths 0.04, 0.02, 0.01, 0.005 and 0.0025, represented by number of nodes in the simulation (solid blue). a1–a6 used adaptive meshes, plotted at the average number of nodes in the simulation, with error bars to indicate the minimum

and maximum number of nodes used during the simulation. The black dots indicates results from NASA-VOF2D (Assier-Rzadkiewicz et al., 1997).

Figure 6: Adaptive mesh at 0.8 seconds in simulation a6. Higher spatial resolution at the boundaries between the three materials can be observed, as can the vertically aligned nature of the mesh.

Figure 7: Geometry and initial condition for Gulf of Mexico test case (Horrillo et al., 2013). There is a vertical exaggeration by a factor of 30.

Figure 8: Density plots at 3, 7 and 10 minutes in SEDFS, MM2FS and MM3 simulations. There is a vertical exaggeration by a factor of 30.

Figure 9: Water surface elevations at 3 minutes, 7 minutes, and 10 minutes for (left) Fluidity: SEDFS (solid red), MM2 (dashed blue), MM3 (solid green), and (right) the range of Fluidity wave heights (yellow area bounded by black line), TSUNAMI3D (solid blue) and FLOW3D (solid red) (from Horrillo et al. (2013)).

Figure 10: Maximum water surface elevations at 3 mins (a) and 7 mins (b) for MM3 simulations. Fixed mesh results for element edge lengths in horizontal/vertical: 400 $\times$ 40 m, 200 $\times$ 20 m, 100 $\times$ 10 m, 50 $\times$ 5 m, 20 $\times$ 2 m and 10 $\times$ 1 m. These are represented by number of nodes in each simulation (solid blue). h1-h4 used adaptive meshes, plotted at the average number of nodes in the simulation, with error bars to indicate the minimum

and maximum number of nodes used. The red dot indicates a result from FLOW3D, with the black dot a result from TSUNAMI3D (Horrillo et al., 2013).

Figure 11: Close up section of adapted mesh at 7 minutes for MM3 simulation h1.

10. Figures

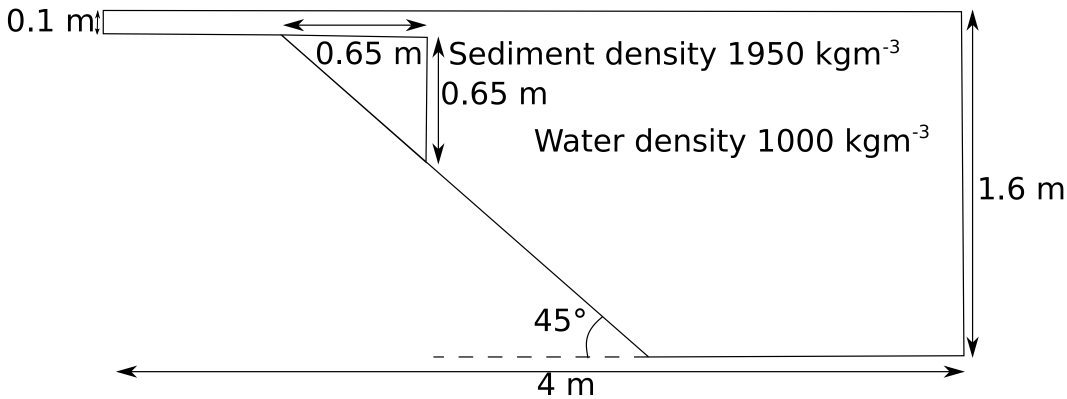

Figure 1:

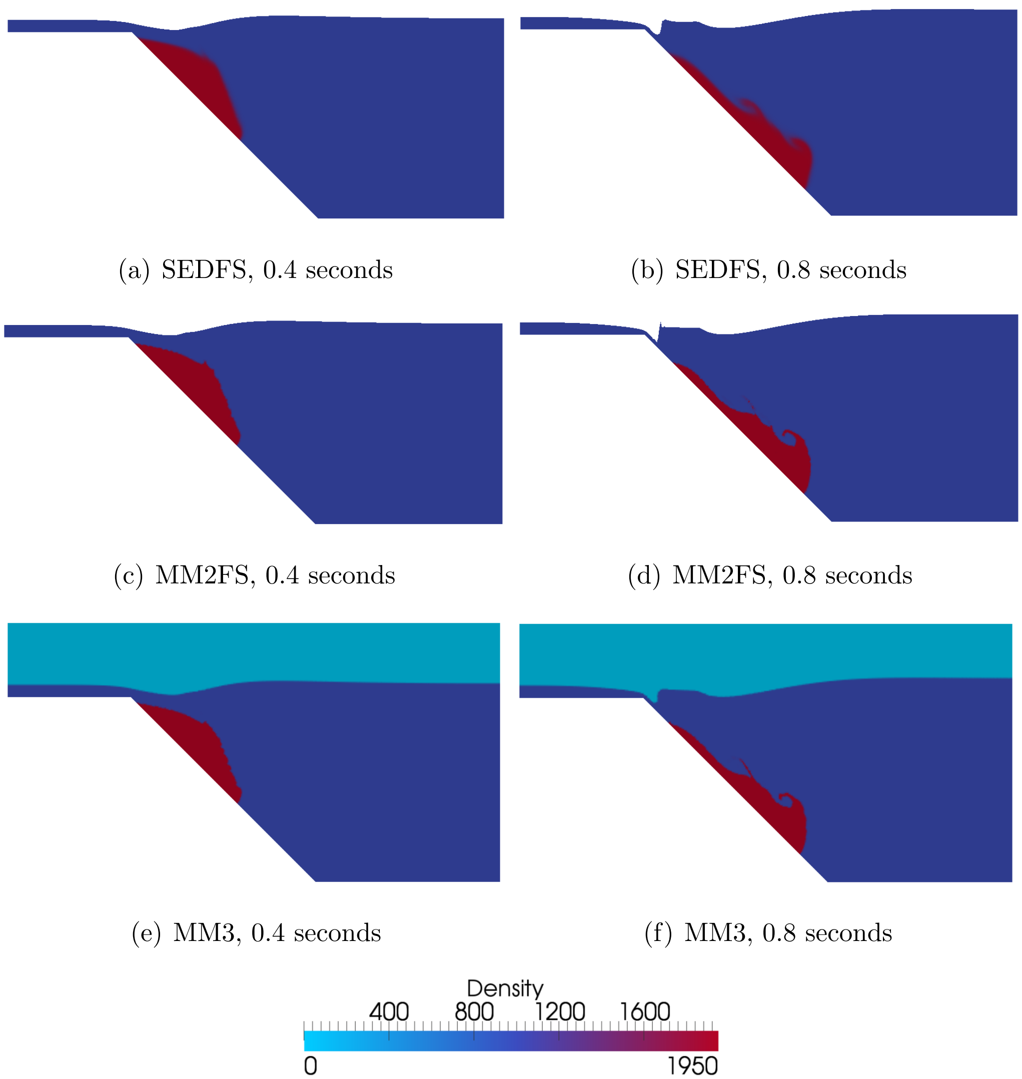

(a) SEDFS, 0.4 seconds

(b) SEDFS, 0.8 seconds

(c) MM2FS, 0.4 seconds

(d) MM2FS, 0.8 seconds

(e) MM3, 0.4 seconds

(f) MM3, 0.8 seconds

Figure 2:

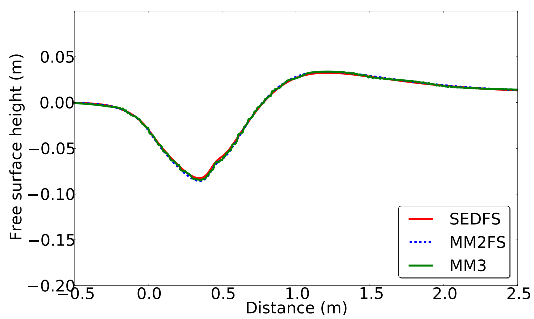

(a) 0.4 seconds

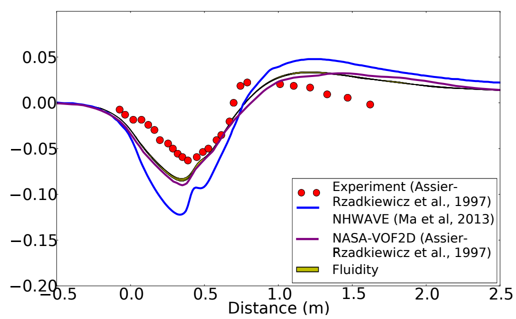

(b) 0.4 seconds

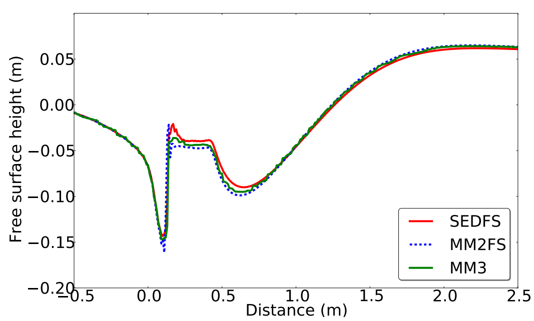

(c) 0.8 seconds

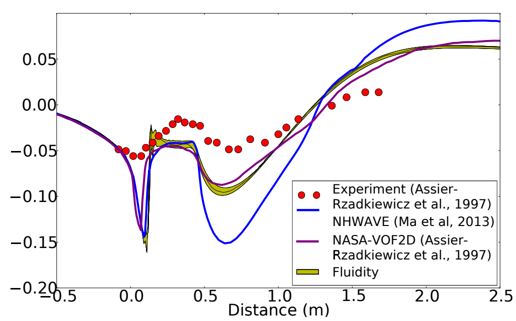

(d) 0.8 seconds

Figure 3:

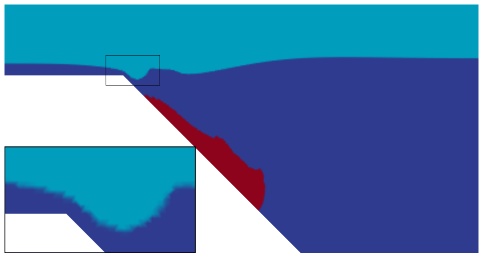

(a) 0.7 seconds

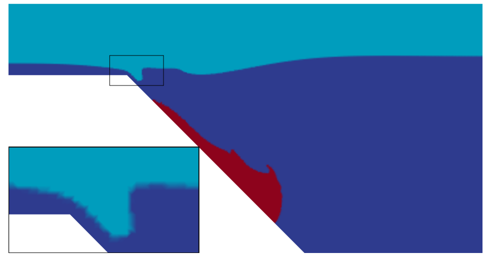

(b) 0.8 seconds

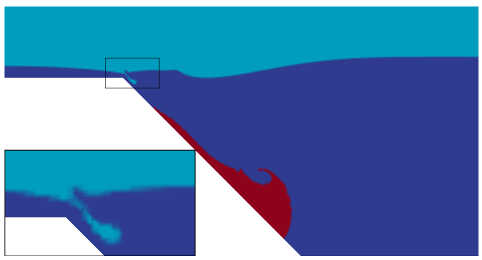

(c) 0.9 seconds

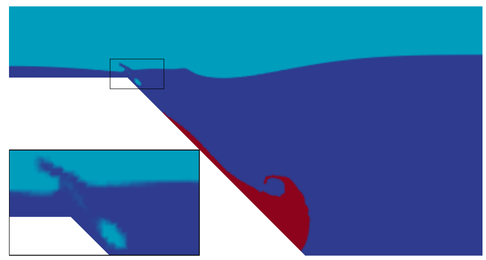

(d) 1.0 seconds

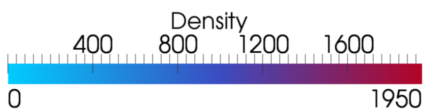

Figure 4:

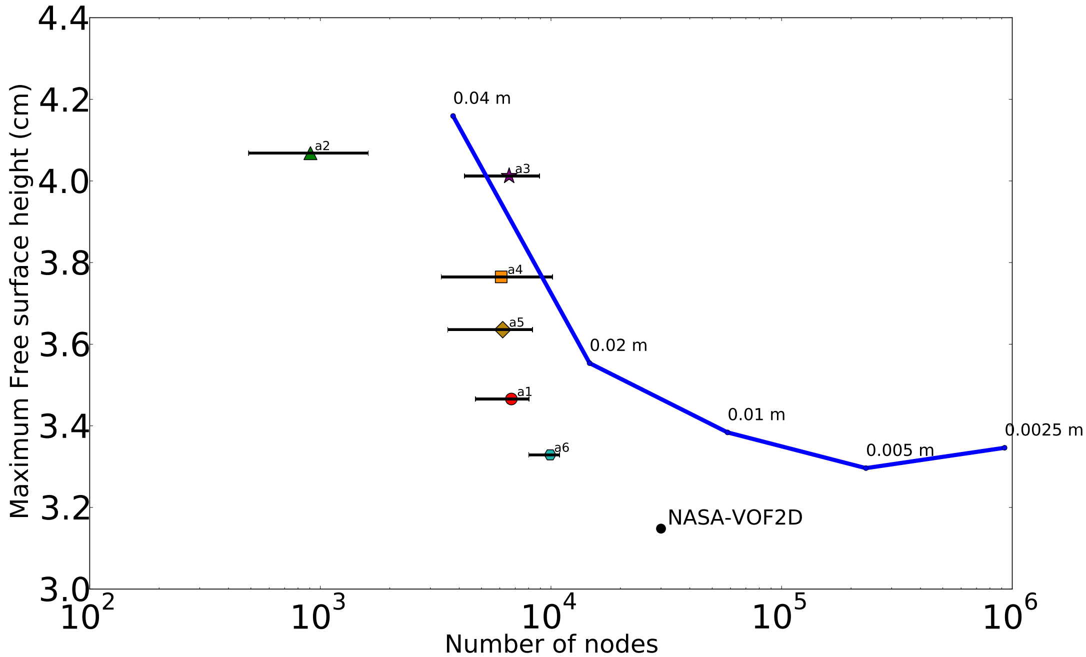

(a) 0.4 seconds

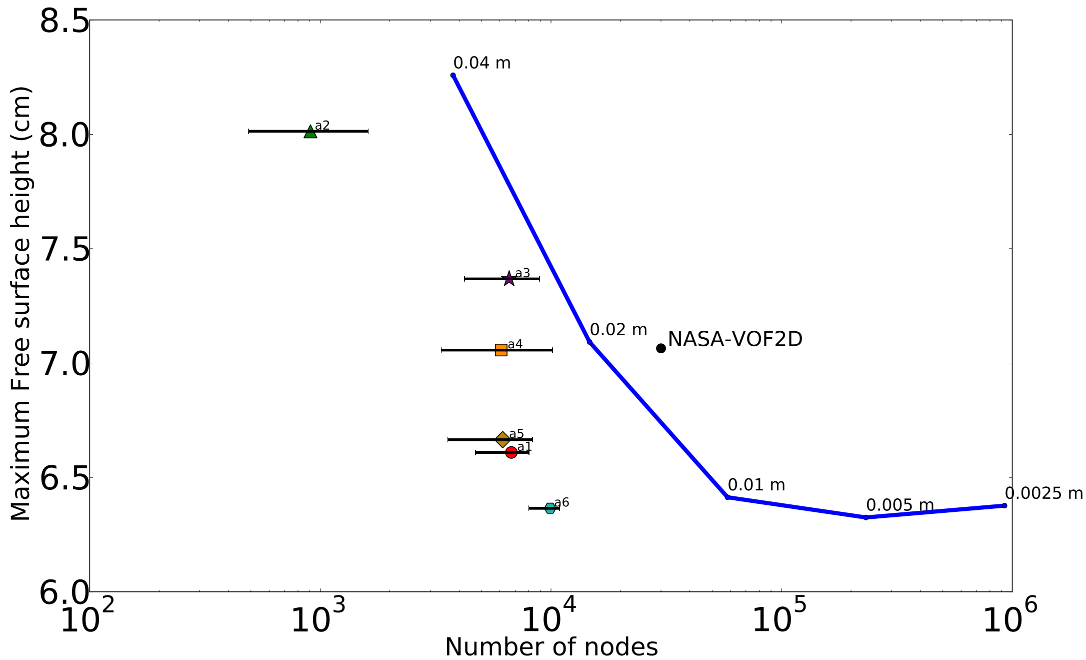

(b) 0.8 seconds

Figure 5:

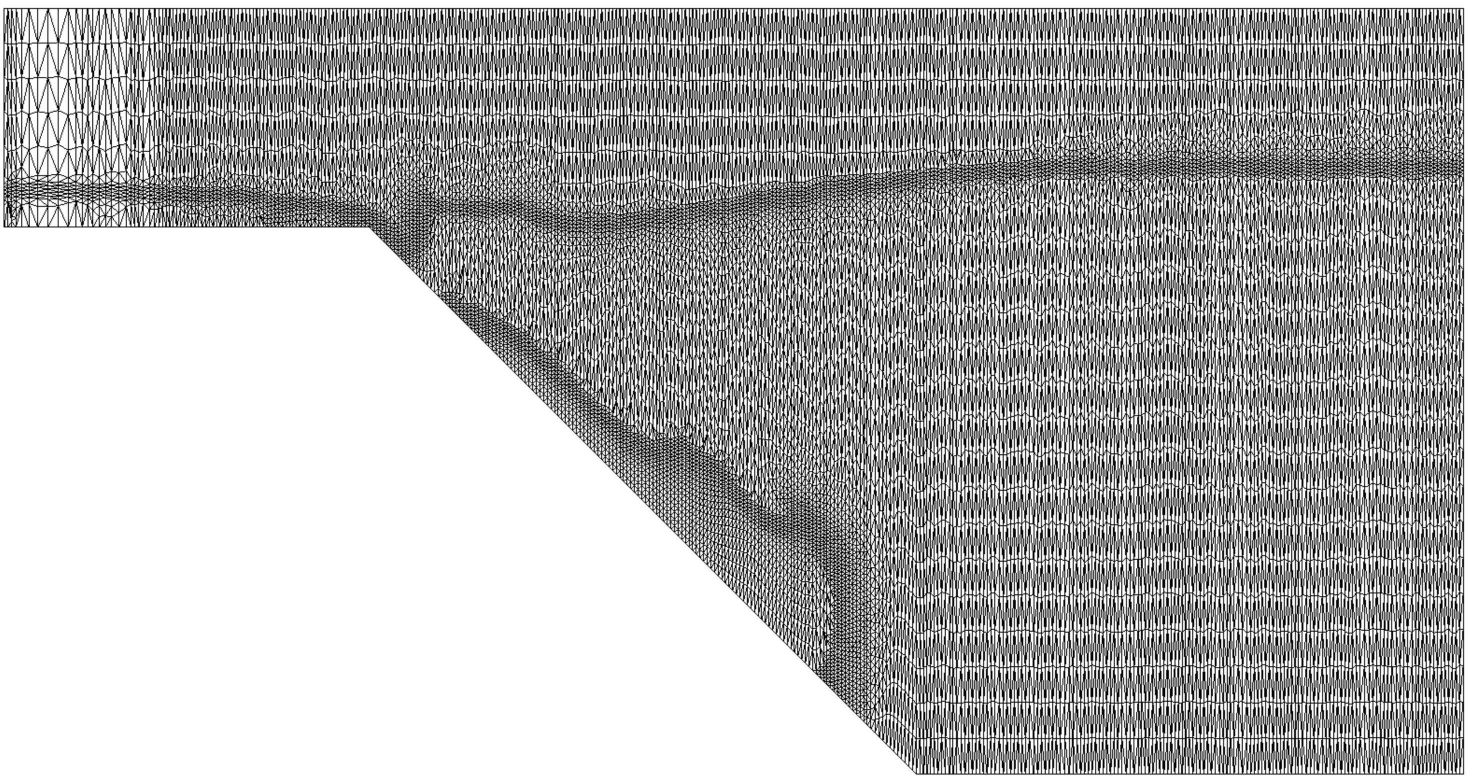

Figure 6:

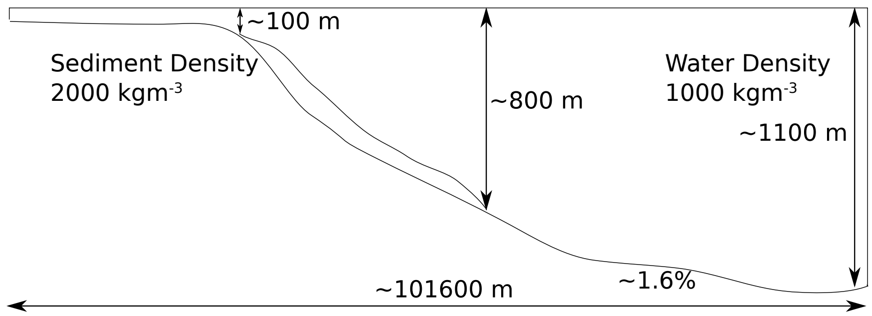
~100 m
Sediment Density
2000 kgm-3
~800 m
Water Density
1000 kgm-3
~1100 m
~101600 m
~1.6%

Figure 7:

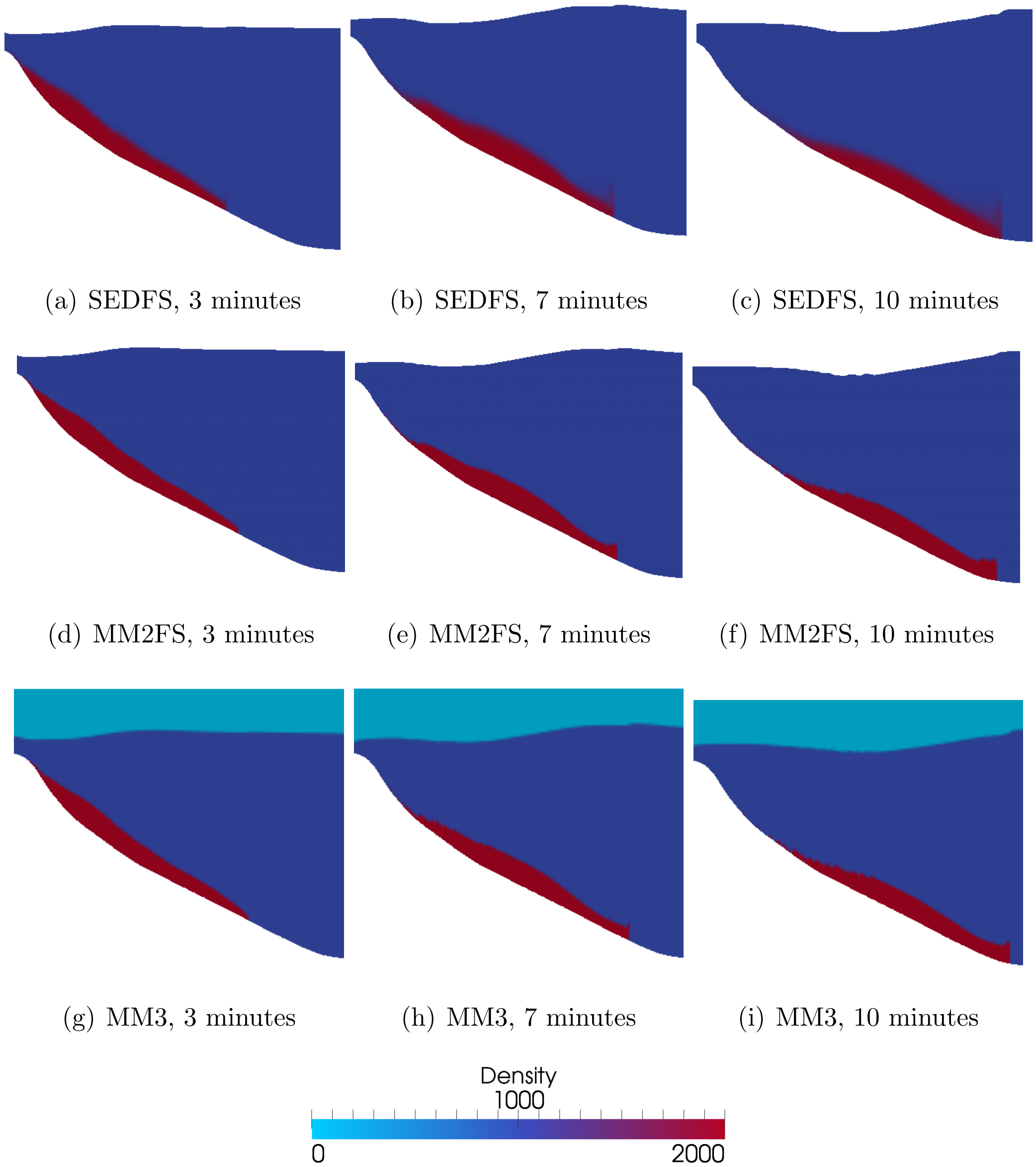

(a) SEDFS, 3 minutes (b) SEDFS, 7 minutes (c) SEDFS, 10 minutes

(d) MM2FS, 3 minutes (e) MM2FS, 7 minutes (f) MM2FS, 10 minutes

(g) MM3, 3 minutes (h) MM3, 7 minutes (i) MM3, 10 minutes

Figure 8:

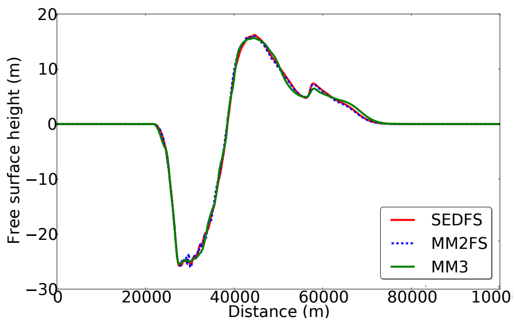

(a) 3 minutes

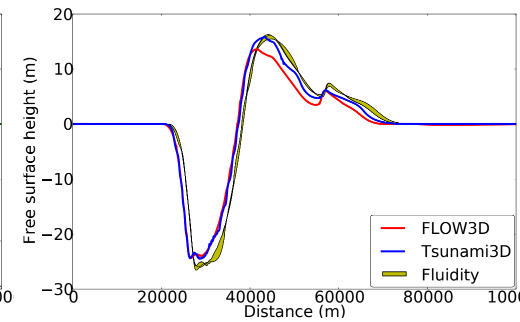

(b) 3 minutes

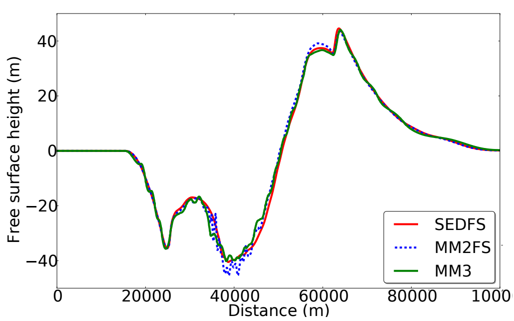

(c) 7 minutes

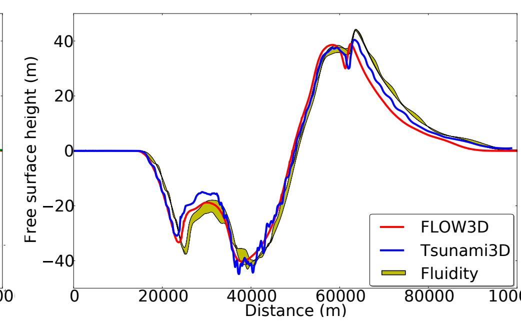

(d) 7 minutes

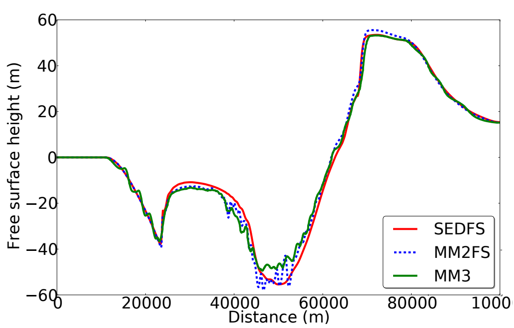

(e) 10 minutes

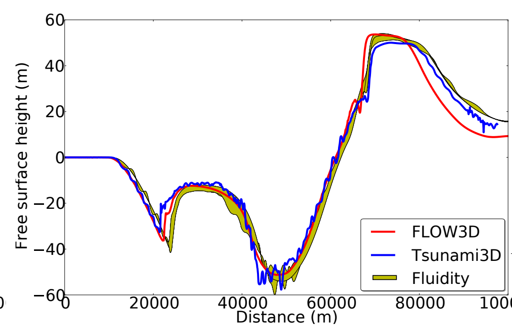

(f) 10 minutes

Figure 9:

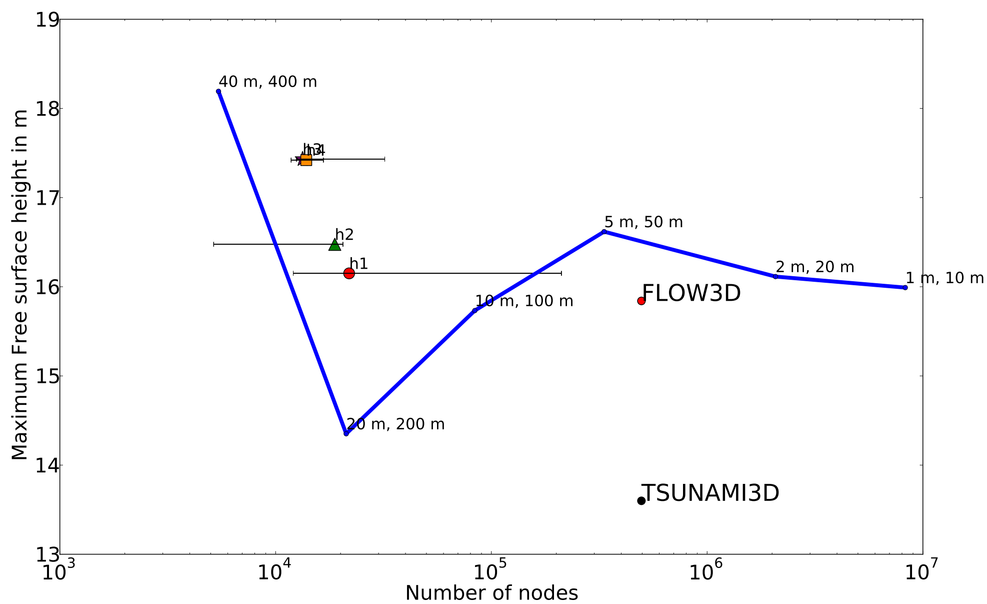

(a) 3 minutes

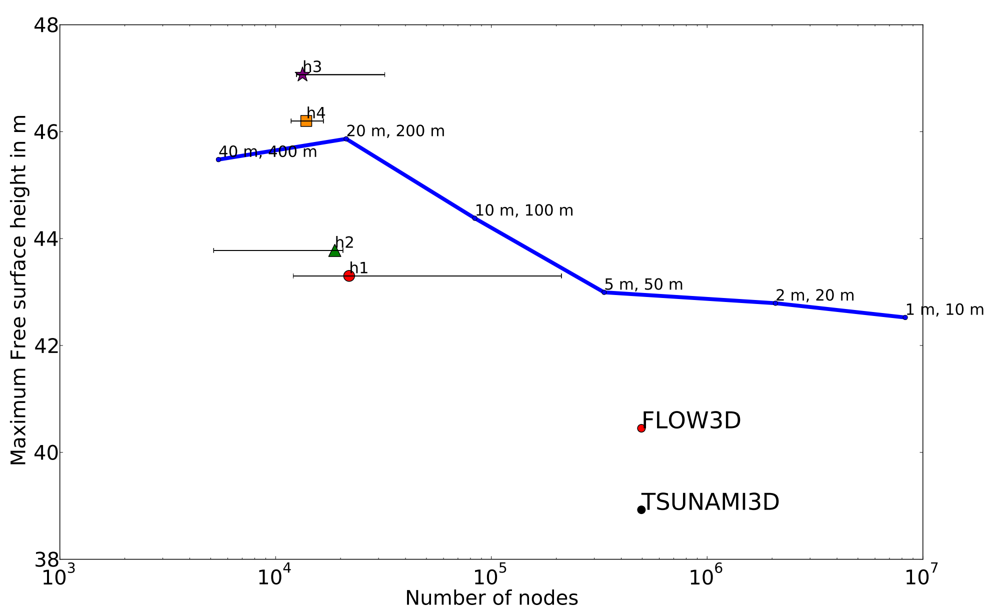

(b) 7 minutes

Figure 10:

.

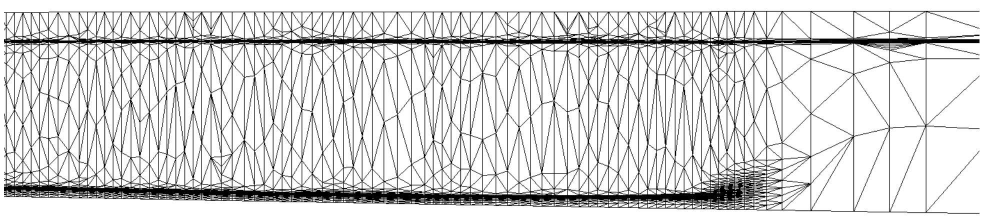

Figure 11: